



Jiang, H., Kammler, M., Ding, F., Dorenkamp, Y., Manby, F. R., Wodtke, A. M., Miller, T. F., Kandratsenka, A., & Bünermann, O. (2019). Imaging covalent bond formation by H atom scattering from graphene. *Science*, 364(6438), 379-382. <https://doi.org/10.1126/science.aaw6378>

Peer reviewed version

License (if available):
Other

Link to published version (if available):
[10.1126/science.aaw6378](https://doi.org/10.1126/science.aaw6378)

[Link to publication record in Explore Bristol Research](#)
PDF-document

This is the accepted author manuscript (AAM). The final published version (version of record) is available online via Science at <https://doi.org/10.1126/science.aaw6378> . Please refer to any applicable terms of use of the publisher.

University of Bristol - Explore Bristol Research

General rights

This document is made available in accordance with publisher policies. Please cite only the published version using the reference above. Full terms of use are available: <http://www.bristol.ac.uk/red/research-policy/pure/user-guides/ebr-terms/>

1 **Imaging covalent bond formation by H-atom scattering** 2 **from Graphene**

3
4
5
6 Hongyan Jiang^{1,2†}, Marvin Kammler^{1,2†}, Feizhi Ding³, Yvonne Dorenkamp^{1,2}, Frederick R. Manby⁴,
7 Alec. M. Wodtke^{1,2,5*}, Thomas F. Miller III^{3*}, Alexander Kandratsenka^{2*}, Oliver Bünermann^{1,5*}

8 **Affiliations:** ¹Institute for Physical Chemistry, Georg-August University of Göttingen, Tam-
9 mannstraße 6, 37077 Göttingen, Germany. ²Department of Dynamics at Surfaces, Max Planck Insti-
10 tute for Biophysical Chemistry, Am Faßberg 11, 37077 Göttingen, Germany. ³Division of Chemistry
11 and Chemical Engineering, California Institute of Technology, Pasadena, CA 91125, USA. ⁴School of
12 Chemistry, University of Bristol, Bristol BS81TS, UK, ⁵International Center for Advanced Studies of
13 Energy Conversion, Georg-August University of Göttingen, Tammannstraße 6, 37077 Göttingen,
14 Germany,

15 **Author Contributions:**

16 †These authors contributed equally to this project.

17 *All correspondence and requests for materials related to this study should be addressed to
18 Oliver Bünermann (Email: Oliver.buenermann@chemie.uni-goettingen.de), Thomas F. Mil-
19 ler III (Email: tfm@caltech.edu), Alexander Kandratsenka (Email: akandra@gwdg.de) and
20 Alec M. Wodtke (Email: alec.wodtke@mpibpc.mpg.de)

21

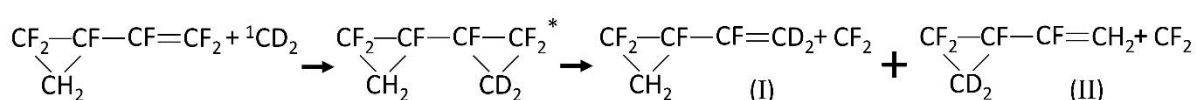
22

23 **Abstract**

24 Viewing the atomic scale motion and energy dissipation pathways involved in forming a co-
25 valent bond is a long standing challenge for chemistry. Here, we perform scattering experi-
26 ments of H atoms from graphene and observe a bimodal translational energy loss distribution.
27 Using accurate first-principles dynamics simulations we show that the quasi-elastic channel
28 involves scattering through the physisorption well where collision sites are near the centers of
29 the six-membered C-rings. The second channel results from transient C-H bond formation,
30 where H-atoms lose 1-2 eV of energy within a 10 *fs* interaction time. This remarkably rapid
31 form of intramolecular vibrational relaxation results from the C atom's re-hybridization dur-
32 ing bond formation and is responsible for an unexpectedly high sticking probability of H on
33 graphene.

34 **Introduction**

35 When a free-radical collides with an unsaturated molecule, electronic re-hybridization may
 36 lead to formation of an addition complex with a great deal of energy initially localized in the
 37 newly formed chemical bond. The addition complex is intrinsically unstable and may re-
 38 dissociate; however, energy flow from the reactive site to the rest of the molecule can delay
 39 this, allowing for isomerization, dissociation of other bonds or stabilizing collisions. Natural-
 40 ly, there has been great interest to observe such energy flow in an addition complex, called
 41 intramolecular vibrational redistribution (IVR). In the classic work of Rynbrandt and Rab-
 42 inovitch, IVR within an addition complex was indirectly detected in the following reaction.



43
 44
 45 After ${}^1\text{CD}_2$ addition, energy is initially localized in only a part of the molecule (indicated by
 46 a *). Before IVR is complete, one expects dissociation to produce excess (I), otherwise similar
 47 amounts of (I) and (II) would form. By varying the pressure of an inert buffer gas and observ-
 48 ing the branching between (I) and (II), the rate of energy flow could be determined. At the
 49 highest buffer gas pressures used, CF_2 elimination occurred faster than ~ 1 ps after formation
 50 of the addition complex. (At longer times the buffer gas quenched the energetic addition com-
 51 plex.) Under these conditions, excess (I) resulted. When longer times for reaction were al-
 52 lowed at lower buffer gas pressures, equal amounts of (I) and (II) were formed. This work
 53 remains some of the strongest evidence that IVR proceeds in an addition complex within a
 54 few ps (1).

55 Since then, IVR experiments with ultrafast PUMP-PROBE spectroscopy proliferated, where
 56 short laser pulses were used to excite specific vibrational motions in stable molecules and
 57 probe the rate of energy flow to other degrees of freedom (2). High-resolution spectroscopy
 58 also helped identify the pathways of energy flow out of initially highly excited C-H stretching
 59 motion (3). This large body of work (4, 5) confirmed that IVR proceeds on a ps time-scale
 60 through a hierarchy of intramolecular processes involving gateway states (6) and bottlenecks
 61 (7). Unfortunately, these spectroscopy experiments cannot tell us about the bond formation
 62 process necessary to produce the addition complex.

63 Scattering experiments can directly probe collision complexes (8) and even reaction reso-
 64 nances whose lifetimes are only a few fs (9, 10). In these studies, researchers produce a beam
 65 of the incident free radicals with well-defined speed and direction. The speed and angular

66 distributions produced by the scattering are then analyzed with first principles simulations.
67 Scattering experiments and molecular dynamics simulations have also been used to develop
68 an atomic-level understanding of energy transfer, accommodation, and reactions during colli-
69 sions between gases and model organic surfaces (11). Scattering free radicals from surfaces
70 allows collision alignment and removes the influence of impact angular momentum, further
71 improving the fruitful interplay between experiment and theory (12, 13). To date, however,
72 scattering studies have never directly probed the direct interplay between chemical bond for-
73 mation and vibrational energy relaxation dynamics.

74 H atom chemisorption to graphene is relevant to hydrogen storage (14), the catalytic produc-
75 tion of molecular hydrogen in the interstellar medium (15) and two-dimensional semiconduc-
76 tor materials, because hydrogenation of graphene can induce a bandgap (16). For the purposes
77 of this study, H adsorption to graphene exhibits the most important features associated with
78 formation of an addition complex, namely re-hybridization during bond formation.

79 Figure 1 shows a 2D cut through a high dimensional potential energy surface (PES) devel-
80 oped in this work. Here, embedded mean-field theory (EMFT) electronic structure data (17-
81 19) is fitted with a reactive empirical bond order (REBO) function (20). See SI methods for
82 details of the PES. H approach to graphene leads to chemical bond formation coincident with
83 sp^2 to sp^3 re-hybridization of a C atom. This is reflected in the binding well being displaced
84 along the C_z coordinate. The structural distortion induced by the electronic re-hybridization
85 gives rise to a barrier - if the H cannot overcome this barrier, the H atom will be reflected
86 (blue trajectory) without inducing re-hybridization. Alternatively, it may pass over the barrier,
87 induce re-hybridization and become trapped (gold trajectory) or scatter back to the gas phase
88 (black trajectory).

89 In this paper, we report H atom scattering experiments with graphene surfaces near zero cov-
90 erage, which removes well-known ambiguities (21) associated with the energy and coverage
91 dependence of C-H bond formation (22). H-atom scattering distributions resolve themselves
92 into a quasi-elastic and a strongly inelastic channel, determined by whether the barrier to
93 chemical bond formation is overcome. The observed inelastic energy transfer distributions
94 contain information about the rate of energy flow out of the newly formed C-H bond. By
95 comparing to molecular dynamics simulations carried out with a full-dimensional PES fit to
96 electronic structure data from a novel and accurate quantum embedding theory (17), we reveal
97 an energy loss mechanism able to remove electron volts of energy from the H atom within the
98 ~ 10 fs of a single-bounce collision. This surprisingly efficient energy flow out of a newly

99 formed chemical bond leads to unexpectedly high sticking probabilities of H on graphene. We
100 show that it is a result of electronic re-hybridization typical of bond formation leading to a
101 covalently bound addition complex.

102 **Results**

103 Figures 2A-C show experimental scattering distributions, $P(E_S; \vartheta_S)$, for collisions of H with
104 graphene grown on a Pt(111) substrate at an incidence energy of 1.92 eV. Pt was chosen as it
105 interacts weakly with graphene (23). Two scattering channels appear with narrow angular
106 distributions peaking close to the specular angle typical of direct “single-bounce” scattering.
107 The quasi-elastic ($E_S/E_I \sim 1$) “fast” channel dominates for large incidence angles, ϑ_I , and
108 gives way to a highly inelastic ($E_S/E_I \sim 0.5$) “slow” channel at small ϑ_I . First principles sim-
109 ulations - Fig.’s 2D-F - agree well with experiment and by analyzing trajectories - Fig. 2G -
110 we find that the slow channel results from trajectories forming a transient C-H bond, whereas
111 the fast channel arises from trajectories that failed to pass over the barrier to bond formation.
112 As ϑ_I decreases, H-atoms more easily cross the barrier, causing the slow channel to grow in
113 importance. This is further evidence for formation of a transient C-H bond that is most favor-
114 ably oriented at 90° to the graphene plane, formed efficiently with normal kinetic energy. We
115 also note that the total scattering signal drops in both experiment and simulation as ϑ_I de-
116 creases. This is partly a result of enhanced scattering out of the plane of detection in the slow
117 channel - see SI sec. S3, Fig. S7. It is also due to enhanced H atom sticking to the graphene
118 surface. Figure 3 shows the experimentally derived sticking probabilities, which increase with
119 the normal component of incidence energy. Here, we lowered E_I to 0.99 eV where sticking is
120 the fate of all H atoms that cross the barrier to C-H bond formation - See SI section S4, Fig.’s
121 S10&11. Under these conditions, only the quasi-elastic channel remains, for which out-of-
122 detection-plane scattering is more easily accounted for and measured survival probabilities
123 lead directly to reliable sticking probabilities. Theoretical simulations of sticking (black sym-
124 bols) are in excellent agreement with experiment - both show efficient sticking even at high
125 incidence energies and an adsorption threshold at $E_n \sim 0.4$ eV reflecting the influence of the
126 barrier to chemisorption.

127 There have been many theoretical predictions of the height of the barrier to C-H bond for-
128 mation on graphene (24, 25); up to now, no experimental validation has been possible. The
129 fact that our dynamical simulations agree well with experimental sticking probabilities argues
130 that the EMFT-REBO PES employed here is accurate. Fig. S2 shows the minimum energy
131 path for C-H bond formation comparing the EMFT-REBO PES to several other calculations

132 all for free standing graphene. We note that both the chemisorption well depth and the barrier
133 height found on the EMFT-REBO PES compare well with values found with CCSD(T) calcu-
134 lations of H addition to coronene (24).

135 The small deviations between experiment and simulation seen in Fig. 3 could be due to re-
136 maining errors in the PES, deficiencies in our treatment of the influence of Pt, which for ex-
137 ample does not properly treat C-Pt bond formation, or the classical approximation. Ring pol-
138 ymer molecular dynamics (26, 27) - open symbols in Fig. 3 - suggest that the net effect of
139 nuclear quantum effects are modest under the conditions studied here, in agreement with pre-
140 vious analysis (28). We also show calculated sticking probability curves with and without the
141 influence of the Pt substrate in Fig. S6 in SI sec. S2, suggesting also that the influence of Pt is
142 small.

143 **Discussion**

144 Figure 4 presents an analysis of trajectories to better understand the H atom translational en-
145 ergy loss and sticking mechanisms. Figure 4A shows that inelastic scattering is dominated by
146 ultrashort single-bounce events. The distribution of times spent within the chemisorption well
147 for the red and blue trajectories of Fig. 1G peaks at only ~ 10 fs - double bounce collisions can
148 also be seen clustered near 22 fs. Despite this, the H-atom energy loss is large. Fig. 4B pro-
149 vides additional insight; here the curves are averages over the subset of (60) trajectories for
150 which the H atom collides on top of a C atom. The kinetic energy that is lost from the incom-
151 ing H atom appears as increased kinetic and potential energy for graphene within 10-20 fs of
152 the initial collision; note that the kinetic energy of that C-atom directly involved in the colli-
153 sion hardly changes.

154 Instead, the neighbors of this C-atom absorb the energy released by transient C-H bond for-
155 mation. Fig. 4E shows the graphene structure, defined in terms of shells. Here, the 0th shell is
156 the C-atom struck by the H atom and the 1st shell reflects the three nearest neighbors. Re-
157 markably, Fig.'s 4C and D show that atoms in the 1st shell pick up kinetic energy first. The
158 creation of an electronically hybridized sp^3 C center during transient C-H bond formation ex-
159 erts strong in-plane forces between the 0th and 1st shell C-atoms. Subsequent to in-plane exci-
160 tation of 1st shell atoms, the H atom induces the 0th shell C atom to pucker out of the plane,
161 only fully experiencing the attractions of a sp^3 -hybridized C-H bond once the puckering has
162 occurred and as the H atom is leaving. The SI contains an animation that shows the interaction
163 energy throughout a typical trajectory, revealing a bonding well is formed only at $t > 0$, where
164 the H atom is recoiling back from the repulsive wall. After departure of the H atom, the de-

165 posited energy flows outward from the region of impact at close to the in-plane speed of
166 sound of graphene (29). See SI section S6, Fig. S16.

167 The large inelasticity seen in the slow channel is peculiar to a network of covalently bound
168 atoms, where C-H bond formation induces forces between multiple C-atoms by a disruption
169 of the delocalized covalent bonding network. This contrasts starkly with the interactions in the
170 fast, quasi-elastic channel - see SI section S7. Here, the H atom interacts with graphene
171 through van der Waals forces, which do not disturb the bonding between C-atoms of the gra-
172 phene. The most probable collision site giving rise to this kind of scattering is near the center
173 of the six-membered C-ring, where chemical bond formation is least likely. See Fig. S18.
174 Hence, the inelasticity in the fast channel follows the predictions of the hard cube model,
175 where the cube has the mass of 5-6 C atoms - see Fig. S17.

176 Next, we use our experimentally validated theoretical model to predict sticking under condi-
177 tions where it is difficult to measure. Theoretical simulations at $E_I = 1.92$ eV show large
178 sticking probabilities (Fig. 3 red symbols). Trapping is efficient, even for H atoms more than
179 2.5 eV above the potential energy minimum, more than 3x the binding well depth. Both the
180 experimental and simulated results presented in Fig. 3 contradict previous theoretical studies,
181 which predicted much smaller sticking probabilities (28, 30-33). See SI section S9 and Fig.
182 S19. This contradiction reflects deficiencies in previous models arising from reduced dimen-
183 sionality approximations as well as errors in the electronic energies produced by DFT at the
184 GGA level. We conclude that, due to the higher accuracy of the electronic energies made pos-
185 sible by the EMFT method and the ability to overcome reduced dimensionality approxima-
186 tions by use of a fitted REBO potential energy surfaces, that the results presented here are the
187 best present knowledge of the sticking probability of H on graphene grown on Pt.

188 This work also provides new insights into the fundamental steps of IVR in a newly formed
189 addition complex. For this analysis, we have also simulated IVR from a highly excited C-H
190 bond to the graphene substrate, for an initially puckered sp^3 hydrogenated graphene structure -
191 see SI section S9. These calculations show that when all energy is initially placed in H kinetic
192 or potential energy, relaxation takes place on two time-scales, with quasi-exponential life-
193 times of 0.5 and 3-4 ps, respectively. A vibrational relaxation time of 5 ps was previously
194 reported for H on graphene (34, 35). These processes reflect the coupling between different
195 vibrational degrees of freedom typical of an anharmonic interaction potential and the time-
196 scales seen here are similar to previous reports about IVR on stable molecules. A particularly
197 surprising aspect of this study is the discovery of a much faster energy loss mechanism requir-

198 ing only 10-20 *fs* to remove 1-2 eV of energy from the newly formed C-H bond. This process
199 proceeds on the time-scale of the C-network deformation induced by sp^2 - sp^3 re-hybridization.
200 There is every reason to believe that this “re-hybridization IVR” plays an important role in the
201 recombination of many covalently bound free radicals forming addition complexes. In partic-
202 ular, we expect re-hybridization IVR to be a strong effect when the structural reorganization
203 associated with complex formation is large - implying the participation of many covalently
204 bound atoms - and when the frequencies associated with the distortion are high, making the
205 time-scale of energy uptake short. We note that in analogy to its important role in determining
206 the sticking probability of H to graphene, re-hybridization IVR is likely to be a determining
207 factor in calculating the collisional formation probability for addition complexes.

208 Supplementary Materials contains information on:

- 209 • **Methods**
 - 210 • **The influence of the Pt substrate on the H atom scattering**
 - 211 • **Out-of-detection-plane scattering**
 - 212 • **H atom sticking probabilities at $E_I = 0.99$ eV**
 - 213 • **A critical comparison of experiment and theory**
 - 214 • **Sonic wave energy transport**
 - 215 • **The hard cube model, the quasi-elastic channel and the site specificity of sticking**
 - 216 • **Comparison to previous sticking probability work**
 - 217 • **Classical simulations of IVR lifetimes**
- 218

219 **Acknowledgements**

220 We thank Dan Auerbach and Dirk Schwarzer for helpful discussions. Funding: HJ, OB and AMW
221 acknowledge support from the SFB1073 under project A04, from the Deutsche Forschungsge-
222 meinschaft (DFG) and financial support from the Ministerium für Wissenschaft und Kultur (MWK)
223 Niedersachsen, and the Volkswagenstiftung under Grant No. INST 186/902-1 to build the experi-
224 mental apparatus. AMW, MK and AK also acknowledge the Max Planck Society for the Advancement
225 of Science. FD and TFM acknowledge that this material is based upon work performed by the Joint
226 Center for Artificial Photosynthesis, a DOE Energy Innovation Hub, supported through the Office of
227 Science of the U.S. Department of Energy under Award No. DE-SC0004993. TFM and FRM
228 acknowledge joint support from the DOE (Award No. DEFOA-0001912). FRM is grateful to the En-
229 gineering and Physical Sciences Research Council for funding (EP/M013111/1). **Authors’ contribu-**
230 **tions:** HJ carried out experiments, analyzed experimental data and contributed to the manuscript. MK
231 participated in the MD and RPMD code development, fit the EMFT data to a REBO potential, carried
232 out molecular dynamics calculations, and contributed to the manuscript. YD assisted with experi-
233 ments. FD contributed to the EMFT code, carried out the EMFT calculations, and contributed to the
234 manuscript. FRM contributed to the EMFT code. AK directed the molecular dynamics work, devel-
235 oped the MD code, and contributed to the manuscript. AMW conceived the experiment and wrote the

236 paper. TFM directed the electronic structure work, contributed to the EMFT code, and contributed to
237 the manuscript. OB built and commissioned the Rydberg tagging apparatus, conceived and supervised
238 experimentation and contributed to the manuscript. **Competing interests:** None declared. **Data and**
239 **materials availability:** The potential energy surface is archived at
240 github.com/akandra/md_tian2/blob/master/src/pes_rebo_mod.f90. There are no restrictions on materi-
241 als used in this work. All data needed to evaluate the conclusions in the paper are present in the paper
242 or the Supplementary Materials.

243

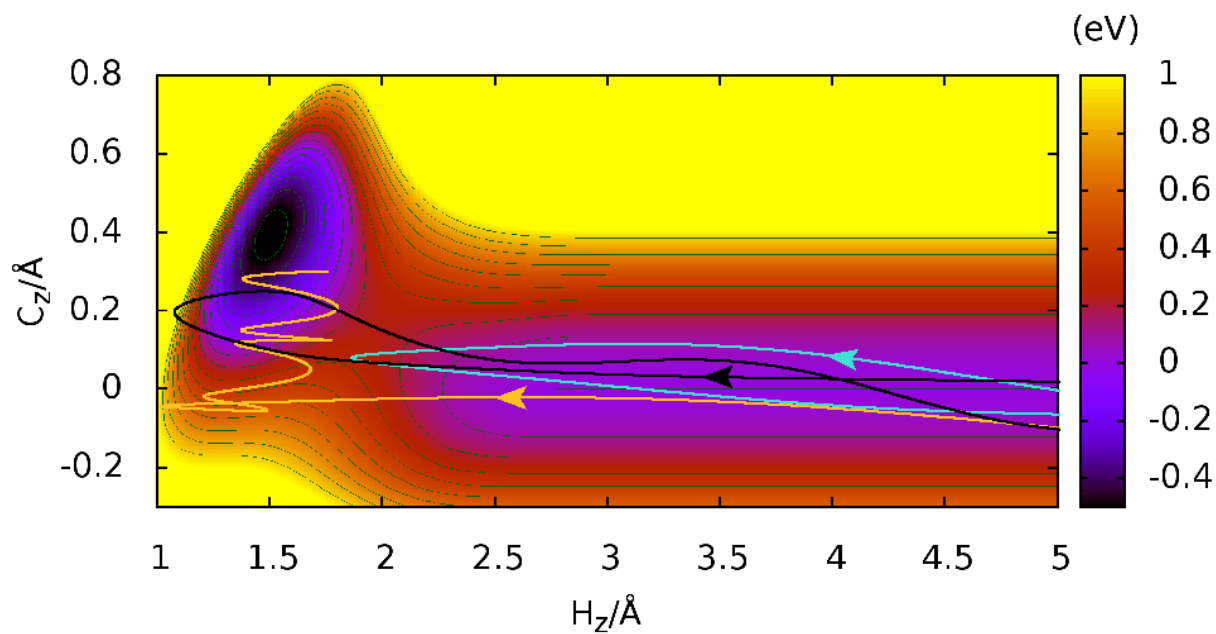


Figure 1: Re-hybridization in the formation of a C-H bond in collisions of an H atom at a graphene surface. H_z and C_z are the distances of the H and C atoms from the graphene plane. Three trajectories are shown for H atoms with 1.92 eV incidence energy.

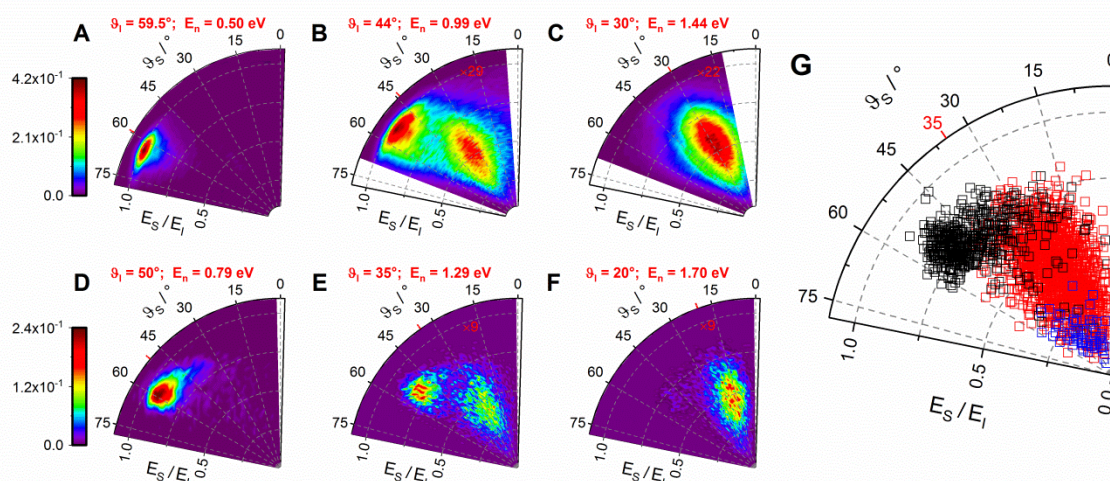


Fig. 2: Bimodal scattering distributions arising from H collisions with graphene. A-C show measured H atom scattering energy, E_S , and angular, ϑ_S , distributions with $E_I = 1.92$ eV. Results for three incidence angles, ϑ_I , are shown. Thus, the normal component of incidence energy, E_n , varies from 0.5 eV to 1.4 eV. $\vartheta_S = 0$ indicates the surface normal direction. Red ticks indicate the specular scattering angles. All observed scattering occurs within 2.8° of the plane defined by incident H atom beam and the surface normal. D-F show corresponding simulated scattering distributions, each shifted by $\sim 10^\circ$ in incidence angles. This shift is discussed in SI Section S5. Each distribution is multiplied by the indicated red number to use the same color bar. Each image represents one million trajectories. G) Analysis of theoretically calculated trajectories for $E_I = 1.92$ eV and $\vartheta_I = 35^\circ$. Single bounce trajectories are shown as red and black. Those in black do not cross the barrier to chemical bond formation. A small number of multi-bounce collisions (blue) are also seen. The simulations include a modelled treatment of the graphene interactions with Pt. See SI section S2.

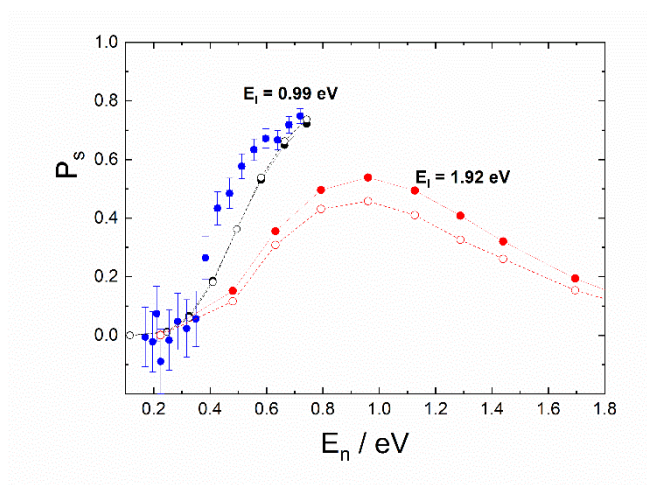


Fig. 3: H atom sticking probabilities at graphene. Experimentally derived (blue) and theoretically predicted (black) sticking probabilities for $E_l = 0.99 \text{ eV}$ plotted against the normal component incidence energy (E_n). Theoretically predicted sticking probabilities for $E_l = 1.92 \text{ eV}$ are shown in red. Theoretical simulations employed a full dimensional EMFT-REBO PES that includes the influence of the Pt substrate with classical molecular dynamics (solid symbols) or ring polymer molecular dynamics (open symbols).

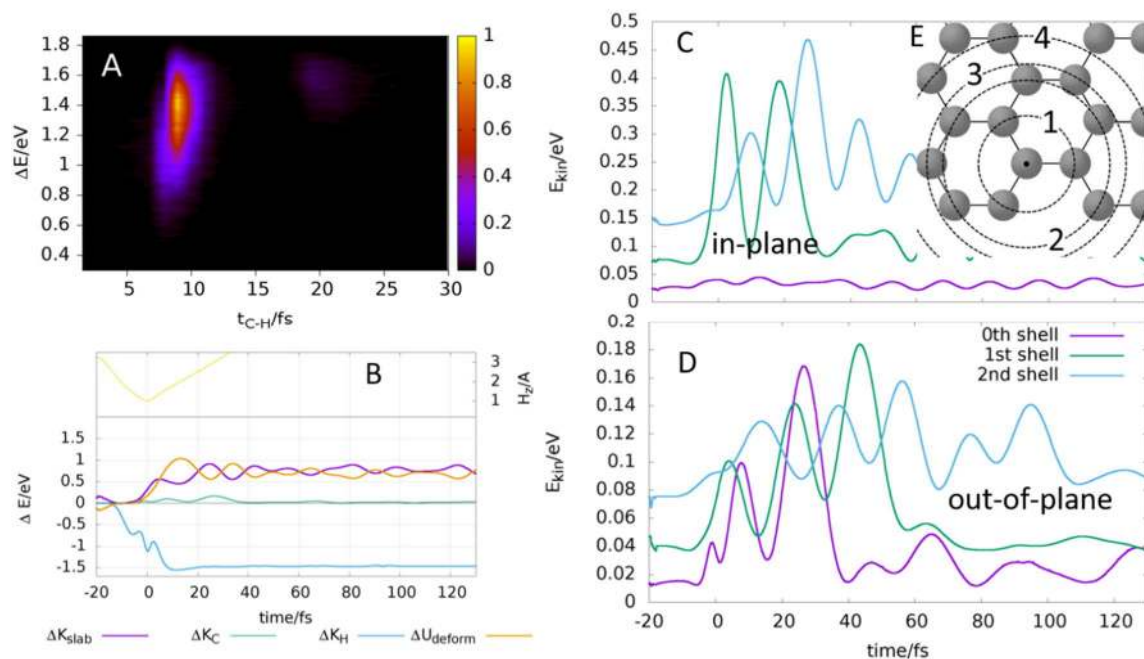


Fig. 4: The dynamical mechanism of energy transfer. **A)** the collision time correlation with H atom energy loss for trajectories that cross the barrier. The collision time is defined as the time spent with a C-H bond distance less than 1.4 \AA . Panels **B**, **C** & **D**, show an average over 60 trajectories that collide on top of a C and pass over the barrier. A collision is labeled *on top* if at the point of closest approach one C-H distance is smaller than 1.15 \AA and three and only three C-H distances are between 1.6 and 2 \AA . $t=0$ is taken as the time of the H atom's closest approach. The incidence conditions are identical to those of Fig. 1G. The yellow curve in **B** shows the H distance to surface, H_z ; single bounce collisions dominate. Also shown are: the kinetic energy change of H atom (ΔK_H , blue); the kinetic energy change of all C atoms, (ΔK_{slab} , purple); the kinetic energy of the C atom hit by the H atom (ΔK_C , green) and the graphene deformation energy, (ΔU_{deform} , gold). Panels **C** and **D** show the kinetic energy appearing in different C-shells. (The shell structure is shown in Panel **E**).

250 **References**

- 251 [1] J. D. Rynbrandt, B. S. Rabinovitch, *Intramolecular energy relaxation - nonrandom*
 252 *decomposition of hexafluorobicyclopropyl*, J. Phys. Chem. **75**, 2164 (1971).
- 253 [2] P. M. Felker, A. H. Zewail, *Direct picosecond time resolution of dissipative*
 254 *intramolecular vibrational-energy redistribution (IVR) in isolated molecules*,
 255 *Chemical Physics Letters* **108**, 303 (1984).
- 256 [3] J. C. Keske, B. H. Pate, *Decoding the dynamical information embedded in highly*
 257 *mixed quantum states*, Annu. Rev. Phys. Chem. **51**, 323 (2000).
- 258 [4] J. D. McDonald, *Creation and disposal of vibrational energy in polyatomic-molecules*,
 259 *Annu. Rev. Phys. Chem.* **30**, 29 (1979).
- 260 [5] M. Gruebele, R. Bigwood, *Molecular vibrational energy flow: beyond the Golden*
 261 *Rule*, International Reviews in Physical Chemistry **17**, 91 (1998).
- 262 [6] D. J. Nesbitt, R. W. Field, *Vibrational energy flow in highly excited molecules: Role of*
 263 *intramolecular vibrational redistribution*, J. Phys. Chem. **100**, 12735 (1996).
- 264 [7] A. A. Stuchebrukhov, R. A. Marcus, *Theoretical-study of intramolecular vibrational-*
 265 *relaxation of acetylenic CH vibration for $\nu = 1$ and 2 in large polyatomic-molecules*
 266 *(CX_3)₃YCCH, where $x = H$ or D and $Y = C$ or SI* , Journal of Chemical Physics **98**,
 267 6044 (1993).
- 268 [8] J. M. Parson, Y. T. Lee, *Crossed molecular-beam study of $F+C_2H_4$, C_2D_4* , Journal of
 269 *Chemical Physics* **56**, 4658 (1972).
- 270 [9] T. G. Yang, J. Chen, L. Huang, T. Wang, C. L. Xiao, Z. G. Sun, D. X. Dai, X. M.
 271 Yang, D. H. Zhang, *Extremely short-lived reaction resonances in Cl plus HD ($\nu=1$) ->*
 272 *DCl plus H due to chemical bond softening*, Science **347**, 60 (2015).
- 273 [10] J. Srinivasan, T. C. Allison, D. W. Schwenke, D. G. Truhlar, *Transition state*
 274 *resonances in the reaction $Cl+H_2 \rightarrow HCl+H$* , Journal of Physical Chemistry A **103**,
 275 1487 (1999).
- 276 [11] J. W. Lu, B. S. Day, L. R. Fiegland, E. D. Davis, W. A. Alexander, D. Troya, J. R.
 277 Morris, *Interfacial energy exchange and reaction dynamics in collisions of gases on*
 278 *model organic surfaces*, Prog. Surf. Sci. **87**, 221 (2012).
- 279 [12] O. Buenermann, H. Jiang, Y. Dorenkamp, A. Kandratsenka, S. M. Janke, D. J.
 280 Auerbach, A. M. Wodtke, *Electron-hole pair excitation determines the mechanism of*
 281 *hydrogen atom adsorption*, Science **350**, 1346 (2015).
- 282 [13] S. M. Janke, D. J. Auerbach, A. M. Wodtke, A. Kandratsenka, *An accurate full-*
 283 *dimensional potential energy surface for H-Au(111): Importance of nonadiabatic*
 284 *electronic excitation in energy transfer and adsorption*, Journal of Chemical Physics
 285 **143**, 124708 (2015).
- 286 [14] L. Schlapbach, A. Züttel, *Hydrogen-storage materials for mobile applications*, Nature
 287 **414**, 353 (2001).

- 288 [15] L. Hornekaer, A. Baurichter, V. V. Petrunin, D. Field, A. C. Luntz, *Importance of*
289 *surface morphology in interstellar H₂ formation*, *Science* **302**, 1943 (2003).
- 290 [16] R. Balog, B. Jorgensen, L. Nilsson, M. Andersen, E. Rienks, M. Bianchi, M. Fanetti, E.
291 Laegsgaard, A. Baraldi, S. Lizzit, Z. Sljivancanin, F. Besenbacher, B. Hammer, T. G.
292 Pedersen, P. Hofmann, L. Hornekaer, *Bandgap opening in graphene induced by*
293 *patterned hydrogen adsorption*, *Nat Mater* **9**, 315 (2010).
- 294 [17] M. E. Fornace, J. Lee, K. Miyamoto, F. R. Manby, T. F. Miller, *Embedded Mean-*
295 *Field Theory*, *Journal of Chemical Theory and Computation* **11**, 568 (2015).
- 296 [18] F. Ding, F. R. Manby, T. F. Miller, *Embedded Mean-Field Theory with Block-*
297 *Orthogonalized Partitioning*, *Journal of Chemical Theory and Computation* **13**, 1605
298 (2017).
- 299 [19] F. Z. Ding, T. Tsuchiya, F. R. Manby, T. F. Miller, *Linear-Response Time-Dependent*
300 *Embedded Mean-Field Theory*, *Journal of Chemical Theory and Computation* **13**,
301 4216 (2017).
- 302 [20] D. W. Brenner, O. A. Shenderova, J. A. Harrison, S. J. Stuart, B. Ni, S. B. Sinnott, *A*
303 *second-generation reactive empirical bond order (REBO) potential energy expression*
304 *for hydrocarbons*, *Journal of Physics-Condensed Matter* **14**, 783 (2002).
- 305 [21] H. Kim, T. Balgar, E. Hasselbrink, *Is there sp³-bound H on epitaxial graphene?*
306 *Evidence for adsorption on both sides of the sheet*, *Chemical Physics Letters* **546**, 12
307 (2012).
- 308 [22] L. Hornekaer, E. Rauls, W. Xu, Z. Sljivancanin, R. Otero, I. Stensgaard, E.
309 Laegsgaard, B. Hammer, F. Besenbacher, *Clustering of chemisorbed H(D) atoms on*
310 *the graphite (0001) surface due to preferential sticking*, *Physical review letters* **97**,
311 186102 (2006).
- 312 [23] I. Hamada, M. Otani, *Comparative van der Waals density-functional study of*
313 *graphene on metal surfaces*, *Physical Review B* **82**, 153412 (2010).
- 314 [24] Y. Wang, H. J. Qian, K. Morokuma, S. Irlle, *Coupled cluster and density functional*
315 *theory calculations of atomic hydrogen chemisorption on pyrene and coronene as*
316 *model systems for graphene hydrogenation*, *The journal of physical chemistry. A* **116**,
317 7154 (2012).
- 318 [25] S. Casolo, O. M. Lovvik, R. Martinazzo, G. F. Tantardini, *Understanding adsorption*
319 *of hydrogen atoms on graphene*, *Journal of Chemical Physics* **130**, (2009).
- 320 [26] S. Habershon, D. E. Manolopoulos, T. E. Markland, T. F. Miller, III, in *Annual*
321 *Review of Physical Chemistry, Vol 64*, M. A. Johnson *et al.*, Eds. (2013), vol. 64, pp.
322 387-413.
- 323 [27] R. Welsch, K. Song, Q. Shi, S. C. Althorpe, T. F. Miller, III, *Non-equilibrium*
324 *dynamics from RPMD and CMD*, *Journal of Chemical Physics* **145**, 204118 (2016).
- 325 [28] M. Bonfanti, B. Jackson, K. H. Hughes, I. Burghardt, R. Martinazzo, *Quantum*
326 *dynamics of hydrogen atoms on graphene. II. Sticking*, *J Chem Phys* **143**, 124704
327 (2015).

- 328 [29] S. V. Dmitriev, J. A. Baimova, A. V. Savin, Y. S. Kivshar, *Ultimate strength, ripples,*
329 *sound velocities, and density of phonon states of strained graphene*, *Comput. Mater.*
330 *Sci.* **53**, 194 (2012).
- 331 [30] J. Kerwin, B. Jackson, *The sticking of H and D atoms on a graphite (0001) surface:*
332 *the effects of coverage and energy dissipation*, *J Chem Phys* **128**, 084702 (2008).
- 333 [31] S. Cazaux, S. Morisset, M. Spaans, A. Allouche, *When sticking influences H₂*
334 *formation*, *Astronomy & Astrophysics* **535**, A27 (2011).
- 335 [32] F. Karlicky, B. Lepetit, D. Lemoine, *Quantum modelling of hydrogen chemisorption*
336 *on graphene and graphite*, *Journal of Chemical Physics* **140**, 124702 (2014).
- 337 [33] S. Morisset, Y. Ferro, A. Allouche, *Study of the sticking of a hydrogen atom on a*
338 *graphite surface using a mixed classical-quantum dynamics method*, *Journal of*
339 *Chemical Physics* **133**, 10 (2010).
- 340 [34] S. Sakong, P. Kratzer, *Isotopic effect on the vibrational lifetime of the carbon-*
341 *deuterium stretch excitation on graphene*, *Journal of Chemical Physics* **135**, 7 (2011).
- 342 [35] S. Sakong, P. Kratzer, *Hydrogen vibrational modes on graphene and relaxation of the*
343 *C-H stretch excitation from first-principles calculations*, *Journal of Chemical Physics*
344 **133**, 8 (2010).
- 345 [36] O. Buenermann, H. Jiang, Y. Dorenkamp, D. J. Auerbach, A. M. Wodtke, *An*
346 *ultrahigh vacuum apparatus for H atom scattering from surfaces*, *Review of Scientific*
347 *Instruments* **89**, 094101 (2018).
- 348 [37] M. Svensson, S. Humbel, R. D. J. Froese, T. Matsubara, S. Sieber, K. Morokuma,
349 *ONIOM: A multilayered integrated MO+MM method for geometry optimizations and*
350 *single point energy predictions. A test for Diels-Alder reactions and Pt(P(t-*
351 *Bu)(3))(2)+H-2 oxidative addition*, *J. Phys. Chem.* **100**, 19357 (1996).
- 352 [38] D. W. Brenner, *The art and science of an analytic potential*, *Physica Status Solidi B-*
353 *Basic Research* **217**, 23 (2000).
- 354 [39] G. C. Abell, *Empirical chemical pseudopotential theory of molecular and metallic*
355 *bonding*, *Physical Review B* **31**, 6184 (1985).
- 356 [40] J. Tersoff, *New empirical-approach for the structure and energy of covalent systems*,
357 *Physical Review B* **37**, 6991 (1988).
- 358 [41] A. D. Becke, *Density-functional thermochemistry .3. The role of exact exchange*,
359 *Journal of Chemical Physics* **98**, 5648 (1993).
- 360 [42] C. T. Lee, W. T. Yang, R. G. Parr, *Development of the colle-salvetti correlation-*
361 *energy formula into a functional of the electron-density*, *Physical Review B* **37**, 785
362 (1988).
- 363 [43] S. H. Vosko, L. Wilk, M. Nusair, *Accurate spin-dependent electron liquid correlation*
364 *energies for local spin-density calculations - a critical analysis*, *Canadian Journal of*
365 *Physics* **58**, 1200 (1980).

- 366 [44] P. J. Stephens, F. J. Devlin, C. F. Chabalowski, M. J. Frisch, *Ab-initio calculation of*
367 *vibrational absorption and circular-dichroism spectra using density-functional force-*
368 *fields*, J. Phys. Chem. **98**, 11623 (1994).
- 369 [45] T. H. Dunning, *Gaussian-basis sets for use in correlated molecular calculations .I.*
370 *The atoms boron through neon and hydrogen*, Journal of Chemical Physics **90**, 1007
371 (1989).
- 372 [46] J. P. Perdew, K. Burke, M. Ernzerhof, *Generalized gradient approximation made*
373 *simple*, Physical review letters **77**, 3865 (1996).
- 374 [47] S. Grimme, *Semiempirical GGA-type density functional constructed with a long-range*
375 *dispersion correction*, Journal of Computational Chemistry **27**, 1787 (2006).
- 376 [48] P. Hohenberg, W. Kohn, *Inhomogeneous electron gas*, Physical Review B **136**, 864
377 (1964).
- 378 [49] W. J. Hehre, R. F. Stewart, J. A. Pople, *Self-consistent molecular-orbital methods .I.*
379 *Use of gaussian expansions of slater-type atomic orbitals*, Journal of Chemical
380 Physics **51**, 2657 (1969).
- 381 [50] F. R. Manby, T. F. Miller, P. Bygrave, F. Ding, T. Dresselhaus, F. A. Batista-Romero,
382 A. Buccheri, C. Bungey, S. J. R. Lee, R. Meli, K. Miyamoto, C. Steinmann, T.
383 Tsuchiya, M. Welborn, T. Wiles, Z. Williams, *entos: A quantum molecular simulation*
384 *package*, DOI: 10.26434/chemrxiv.7762646 (2019).
- 385 [51] G. Kresse, *Ab-initio molecular-dynamics for liquid-metals*, Journal of Non-Crystalline
386 Solids **193**, 222 (1995).
- 387 [52] G. Kresse, J. Hafner, *Ab-initio molecular-dynamics simulation of the liquid-metal*
388 *amorphous-semiconductor transition in germanium*, Physical Review B **49**, 14251
389 (1994).
- 390 [53] G. Kresse, J. Furthmuller, *Efficiency of ab-initio total energy calculations for metals*
391 *and semiconductors using a plane-wave basis set*, Comput. Mater. Sci. **6**, 15 (1996).
- 392 [54] G. Kresse, J. Furthmuller, *Efficient iterative schemes for ab initio total-energy*
393 *calculations using a plane-wave basis set*, Physical Review B **54**, 11169 (1996).
- 394 [55] P. E. Blöchl, *Projector augmented-wave method*, Physical Review B **50**, 17953 (1994).
- 395 [56] R. Polly, H. J. Werner, F. R. Manby, P. J. Knowles, *Fast Hartree-Fock theory using*
396 *local density fitting approximations*, Molecular Physics **102**, 2311 (2004).
- 397 [57] F. Weigend, *A fully direct RI-HF algorithm: Implementation, optimised auxiliary*
398 *basis sets, demonstration of accuracy and efficiency*, Physical Chemistry Chemical
399 Physics **4**, 4285 (2002).
- 400 [58] H. Shin, S. Kang, J. Koo, H. Lee, J. Kim, Y. Kwon, *Cohesion energetics of carbon*
401 *allotropes: Quantum Monte Carlo study*, Journal of Chemical Physics **140**, 114702
402 (2014).

- 403 [59] B. I. Dunlap, J. C. Boettger, *Local-density-functional study of the fullerenes, graphene*
404 *and graphite*, Journal of Physics B-Atomic Molecular and Optical Physics **29**, 4907
405 (1996).
- 406 [60] I. R. Craig, D. E. Manolopoulos, *Quantum statistics and classical mechanics: Real*
407 *time correlation functions from ring polymer molecular dynamics*, Journal of
408 Chemical Physics **121**, 3368 (2004).
- 409 [61] M. Ceriotti, M. Parrinello, T. E. Markland, D. E. Manolopoulos, *Efficient stochastic*
410 *thermostatting of path integral molecular dynamics*, Journal of Chemical Physics **133**,
411 124104 (2010).
- 412 [62] M. Andersen, L. Hornekaer, B. Hammer, *Graphene on metal surfaces and its*
413 *hydrogen adsorption: A meta-GGA functional study*, Physical Review B **86**, 085405
414 (2012).
- 415 [63] Y. J. Dorenkamp, Ph.D. Thesis, Georg-August University of Goettingen (2018).
- 416 [64] H. C. Andersen, *Molecular-dynamics simulations at constant pressure and-or*
417 *temperature*, Journal of Chemical Physics **72**, 2384 (1980).
- 418 [65] E. Bitzek, P. Koskinen, F. Gahler, M. Moseler, P. Gumbsch, *Structural relaxation*
419 *made simple*, Physical review letters **97**, 170201 (2006).

420 **References for SI**

421 36-65

422

423

424

Supplementary Material for

425 **Imaging covalent bond formation by H-atom scattering** 426 **from Graphene**

427

428 Hongyan Jiang^{1,2†}, Marvin Kammler^{1,2†}, Feizhi Ding³, Yvonne Dorenkamp^{1,2}, Frederick R. Manby⁴,

429 Alec. M. Wodtke^{1,2,5*}, Thomas F. Miller III^{3*}, Alexander Kandratsenka^{2*}, Oliver Bünermann^{1,5*}

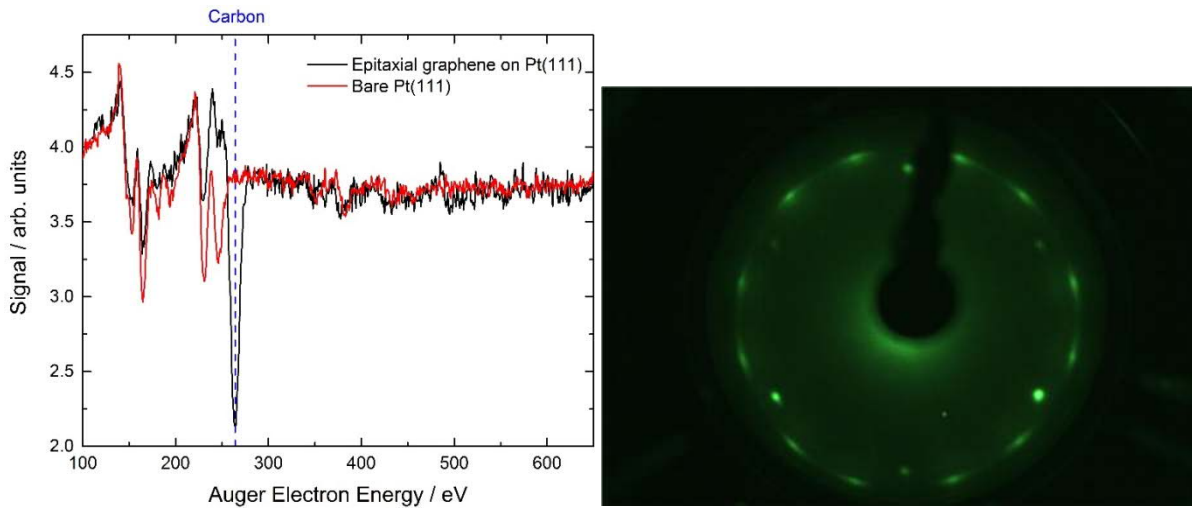
430 **Affiliations:** ¹Institute for Physical Chemistry, Georg-August University of Göttingen, Tam-
431 mannstraße 6, 37077 Göttingen, Germany. ²Department of Dynamics at Surfaces, Max Planck Insti-
432 tute for Biophysical Chemistry, Am Faßberg 11, 37077 Göttingen, Germany. ³Division of Chemistry
433 and Chemical Engineering, California Institute of Technology, Pasadena, CA 91125, USA. ⁴School of
434 Chemistry, University of Bristol, Bristol BS81TS, UK, ⁵International Center for Advanced Studies of
435 Energy Conversion, Georg-August University of Göttingen, Tammannstraße 6, 37077 Göttingen,
436 Germany,

437

438 **S1. Methods**

439 **Experimental procedures**

440 The Pt(111) substrate was cleaned by several cycles of Ar⁺ ion sputtering (30 mins) followed
441 by annealing at 900°C (30 mins) and then flashing to 1000°C (2 mins). Surface cleanliness
442 and structure were checked by Auger electron spectroscopy (AES) and low energy electron
443 diffraction (LEED). The graphene sample was prepared by dosing ethylene on a clean Pt(111)
444 substrate at 700 °C for 15 mins. The ethylene partial pressure was kept at 3×10⁻⁸ mbar during
445 the dosing. The quality of the single layer graphene was confirmed by AES, LEED (Fig. S1)
446 and by the comparison between scattering results from pristine Pt(111) surface and the gra-
447 phene sample.



448

449 **Figure S1: Characterization of graphene sample. (left panel) Auger spectrum of Pt(111) (red)**
450 **and epitaxial graphene grown on Pt(111).** The C Auger electron peak is marked by the blue dashed
451 line. No other elements are detected, indicating the cleanliness of the surfaces. **(right panel) Low**
452 **energy electron diffraction (LEED) spectrum of epitaxial graphene on Pt(111).** Electron incidence
453 energy is 87 eV. The six circular diffraction spots at smaller polar diffraction angles are from Pt(111);
454 three spots are dim and three bright. At slightly larger polar diffraction angles, twelve spots from gra-
455 phene can be seen. Each of two orientational domains in the sample gives rise to six spots. The spots
456 are broadened in the azimuthal direction, due to the weak interaction with Pt, which leads to a distribu-
457 tion of graphene Pt orientations with ~ 5° width.

458 The experimental apparatus has been described in detail in Ref. (36). Nearly mono-energetic
459 hydrogen atom beams are generated by photolyzing a supersonic beam of hydrogen iodide
460 with ArF or KrF excimer laser light. A small fraction of the atoms pass a skimmer, enter the
461 first of two differential pumping chambers and pass into an ultrahigh vacuum chamber, where
462 the graphene sample is held. The graphene is held on a 6-axis manipulator, allowing variation
463 of the incidence angle, ϑ_i . The scattered H atoms are excited to a long lived Rydberg state by
464 two spatially and temporally overlapped laser pulses passing parallel to the sample at a dis-
465 tance of 0.7 mm. The first laser pulse excites the 1s-2p transition at 121.57 nm and the second

466 excites the $2p-n=34$ transition close to 365 nm. The neutral Rydberg atoms travel 250 mm
467 where they are field ionized and detected by an MCP. The arrival time is recorded using a
468 multi-channel scalar. The rotatable detector allows time-of-flight spectra to be recorded at
469 various scattering angles, ϑ_S . The H-atoms' incidence translational energy, E_I , can be con-
470 trolled by changing the photolysis wavelength. The normal component of the incidence trans-
471 lational energy can be varied by changing the incidence angle at a constant E_I .

472 Theoretical methods

473 *General approach: Embedded mean-field theory*

474 Embedded mean-field theory (EMFT) (17-19) provides energies and forces from first-
475 principles for parameterization of the REBO potential. EMFT is an electronic structure em-
476 bedding approach that allows a subset of a system to be described using a relatively more ac-
477 curate but expensive mean-field theory (such as DFT with a hybrid functional and large basis
478 set), while the remainder of the system is described using a lower accuracy and cheaper mean-
479 field level (such as DFT with a LDA functional and a small basis set). In the EMFT method,
480 the subsystems are partitioned in terms of the atom-centered atomic orbital basis. Unlike the
481 ONIOM method (37), EMFT does not require specification of the number of electrons per
482 subsystem, nor does it require specification of the spin-state of the subsystem; only the total
483 number of electrons and the total spin-state of the system is specified. The method is accurate
484 and efficient over a wide range of systems and chemical applications, including those that
485 involve subsystem partitioning across conjugated bonding networks (17-19).

486 *General approach: Reactive empirical bond order potential*

487 The second generation reactive empirical bond order potential (REBO) was developed by
488 Brenner *et al.* (20) to describe various carbon modifications and hydrocarbons with an accu-
489 rate, flexible, transferable and computationally efficient analytic potential (38). It is based on
490 the ideas of Abell and Tersoff who assumed that the binding energy between two atoms can
491 be modeled by the sum of an attractive and a repulsive term (39, 40). The attractive term can
492 either be enhanced or weakened by a bond order factor. While attraction and repulsion is only
493 a function of the distance between two atoms, the bond order term also takes hybridization of
494 the carbon atoms into account. Information about an atoms hybridization is inferred from its
495 surroundings using Abell's argument that the bond order is proportional to the inverse square
496 root of the coordination number. REBO also includes the effects of radical species within a
497 molecular structure as well as rotation about dihedral angles for carbon-carbon double bonds.
498 The interaction range is limited by a cutoff function chosen in such that the nearest neighbors

499 are always accounted for while the second nearest neighbor are fully excluded. The strength
500 of the interaction is determined by multiple quadratic-, cubic- and higher-order, multi-
501 dimensional spline functions. The default parameter set for standard REBO was tuned to re-
502 produce the potential energy surfaces of solid carbon structures and small organic molecules.
503 Although REBO with its default parameter set has been successfully used for many hydrocar-
504 bon configurations, it does not give accurate results for H interactions with graphene. Conse-
505 quently, we used *ab initio* electronic structure data obtained from EMFT to train the parame-
506 ter set for accurate results in this system.

507 *Computational details. 1. Benchmarking the electronic structure methods.*

508 The current section compares the results of various electronic structure methods in describing
509 the binding-energy well depth and barrier height for an H atom interacting with graphene,
510 including the CCSD(T), DFT, EMFT, and EMFT-REBO methods. The CCSD(T) results were
511 previously reported (24). DFT calculations are performed with a hybrid functional using an
512 atom-centered Gaussian-type orbital (GTO) basis (B3LYP/cc-pVDZ) (41-45), as well as with
513 a GGA functional (PBE) (46) with Grimme D2 corrections (47) using a plane-wave basis with
514 a 400 eV cutoff and *k*-point sampling with a gamma-centered mesh of 8x8x1. EMFT results
515 are obtained with a B3LYP/cc-pVDZ description (41-45) for the atoms in the vicinity of the H
516 collision and with an LDA/STO-3G description (43, 48, 49) for the remaining atoms (see *Sec-*
517 *tion SI Computational Details 2* for details), and EMFT-REBO results are obtained using the
518 REBO method to fit the EMFT potential energy points (see *Section SI Computational Details*
519 *3* for details).

520 All EMFT and GTO-based DFT calculations reported in this study are performed using the
521 *entos* molecular simulation package (50). These calculations employ standard self-consistent
522 field (SCF) procedures, including use of superposition of the atomic densities (SAD) as the
523 initial guess, the direct inversion in the iterative subspace (DIIS) algorithm for SCF accelera-
524 tion, and a convergence threshold of 10^{-5} a.u. on the maximum value of the orbital gradient.
525 Plane-wave DFT calculations are performed using the VASP software package (51-54). For
526 the plane-wave calculations, spin polarization is included, and we employ the tetrahedron
527 method with Blöchl corrections (55) to treat partial occupancies with the default smearing
528 parameter of 0.2 eV. Interactions between the core and valence electrons are modeled by the
529 projector augmented wave approach (55). The relaxation of the electronic degrees of freedom
530 is stopped when the change in energy between iterations is smaller than 10^{-5} eV. In the calcu-
531 lations of the minimum energy pathway, convergence of the ionic relaxation loop is reached

532 when all forces are smaller than 10^{-3} eV/Å. The chemisorption well depth and barrier heights
533 are reported in Table S1, and the full MEPs are reported in Figure S2.

Table S1. Calculated chemisorption well depth and barrier height (in eV) for H atom on-top adsorption on graphene at various levels of theory.^a

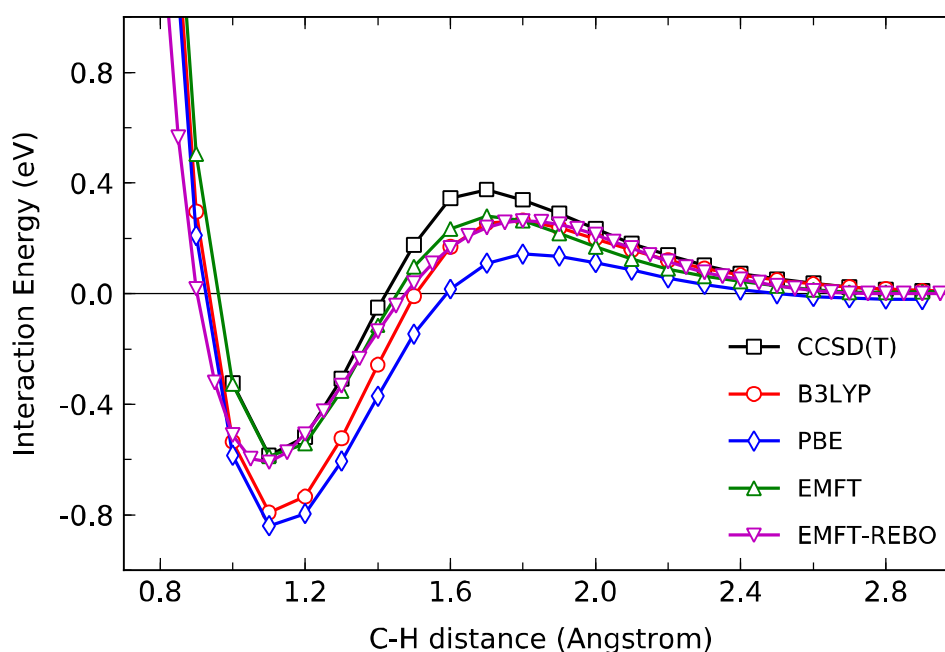
Graphene system	Method	Well depth (eV)	Barrier height (eV)
Coronene	CCSD(T)/cc-pVDZ ^b	-0.58	0.37
$C_{42}H_{16}$	B3LYP/cc-pVDZ	-0.80	0.27
	EMFT ^c	-0.59	0.28
Periodic (3 x 4 unit cell)	PBE/plane-wave	-0.84	0.14
Periodic (3 x 4 unit cell)	EMFT-REBO	-0.61	0.26

534 ^a The energy at dissociation limit is chosen as reference. Zero-point energy corrections are not includ-
535 ed. For finite-system calculations, basis set superposition errors are negligible and thus not included.

536 ^b Ref. (24).

537 ^c High-level : B3LYP/cc-pVDZ; low-level: LDA/STO-3G; Subsystem partitioning shown in Fig. S5.

538



539

Figure S2. Calculated minimum energy path (MEP) for H atom on-top adsorption on free-standing graphene at various levels of theory. The levels of theory reported here are the same as in Table S1.

540

541 For the results in Table S1 and Fig. S2, the following system sizes were employed. The
542 CCSD(T) results (24) were obtained for an H atom interacting with the coronene graphene
543 flake, $C_{24}H_{12}$. The EMFT results and DFT results in the GTO basis were obtained for an H

544 atom interacting with a larger graphene flake, $C_{42}H_{16}$, and using 16 carbon atoms in the high-
545 level subsystem for the EMFT calculations (Fig. S2); additional benchmarking results with
546 larger graphene flakes are presented in *Section SI Computational Details 2*. The plane-wave
547 DFT and EMFT calculations were performed with periodic boundary conditions, using a sim-
548 ulation cell with 24 carbon atoms arranged such that the surface consists of 3 by 4 primitive
549 cells. A vacuum region of 13 Å above the graphene ensures that periodically stacked surfaces
550 do not interact with one another.

551 For the results in Table S1 and Fig. S2, the chemisorption well depth and barrier height are
552 examined in terms of the minimum energy path (MEP) along the on-top approach angle,
553 which corresponds to the H atom approaching the center carbon atom from the direction nor-
554 mal to the graphene surface. The reported DFT B3LYP/cc-pVDZ, PBE/plane-wave, and
555 EMFT-REBO energies are evaluated at geometries that were optimized at the same level of
556 theory; specifically, all degrees of freedom are relaxed at each fixed value for the C-H dis-
557 tance. The reported CCSD(T)/cc-pVDZ and EMFT energies are evaluated at the B3LYP/cc-
558 pVDZ-optimized geometries. The chemisorption well depth is computed as the electronic
559 energy difference between the minimum along this MEP and the system at infinite H-
560 graphene separation distance; the chemisorption barrier height is computed as the electronic
561 energy difference between the maximum along this MEP and the system at infinite H-
562 graphene separation distance.

563 In agreement with previous work (24), it is seen in Table S1 and Fig. S2 that the PBE/plane-
564 wave result underestimates the barrier height for the H-graphene interaction relative to
565 CCSD(T) by over a factor of two, whereas the B3LYP/cc-pVDZ description returns the calcu-
566 lated barrier height to within 0.1 eV of the CCSD(T) result. The EMFT description of the barri-
567 er height is essentially unchanged from that of the more costly B3LYP/cc-pVDZ calculations;
568 the well-depth for the EMFT description at these geometries is slightly lower than that of
569 B3LYP/cc-pVDZ, although it remains close to the CCSD(T)/cc-pVDZ description. Finally,
570 the EMFT-REBO calculations, which are directly parameterized on the basis of the EMFT
571 calculations, precisely reproduce both the EMFT barrier height and well depth. It is particu-
572 larly notable that while the EMFT results are obtained at B3LYP/cc-pVDZ-optimized geome-
573 tries while the EMFT-REBO results are obtained at EMFT-REBO-optimized geometries, the
574 resulting MEPs are essentially identical at all C-H separations; this indicates that the shape of
575 the EMFT-REBO, EMFT, and B3LYP/cc-pVDZ potential energy surfaces are all very simi-
576 lar, as is the goal of the methods. Taken together, these results indicate that the CCSD(T) re-

577 sults are reproduced well using EMFT for this system, and they demonstrate the fidelity with
578 which the EMFT-REBO results reproduce EMFT.

579 *Computational details. 2. EMFT calculation details and benchmarking.*

580 All EMFT calculations in the current study employ B3LYP-in-LDA embedding, with a high-
581 level subsystem described using DFT with the B3LYP hybrid functional (41-44) and the cc-
582 pVDZ basis set (45), while the surrounding environment is described using DFT with the
583 LDA functional (43, 48) and the minimal STO-3G basis set (49). The density-fitting approx-
584 imation with the cc-pVDZ/JKFIT (56) basis is employed for evaluation of the electron repul-
585 sion integrals (57). Both the atomic-orbital and density-fitting basis functions are implement-
586 ed as GTOs. All EMFT calculations are open-shell and employ spin-unrestricted orbitals.
587 Benchmark studies confirm that a graphene flake of $C_{42}H_{16}$ is sufficiently large to describe the
588 H-on-graphene interactions (Fig. S3) and confirm that a high-level subsystem comprised of
589 the colliding H atom and the 16 carbon atoms is necessary (Fig. S4). Based on these bench-
590 mark results, all EMFT results were performed for a system with a graphene flake of $C_{42}H_{16}$
591 using 16 carbon atoms in the high-level subsystem (Fig. S5), as well as including the scatter-
592 ing H in the high-level region. Using these parameters, the computational cost of the B3LYP-
593 in-LDA embedding description using EMFT is vastly reduced (over 11-fold) in comparison to
594 the computational cost of the full calculation performed at the B3LYP/cc-pVDZ level (Table
595 S2).

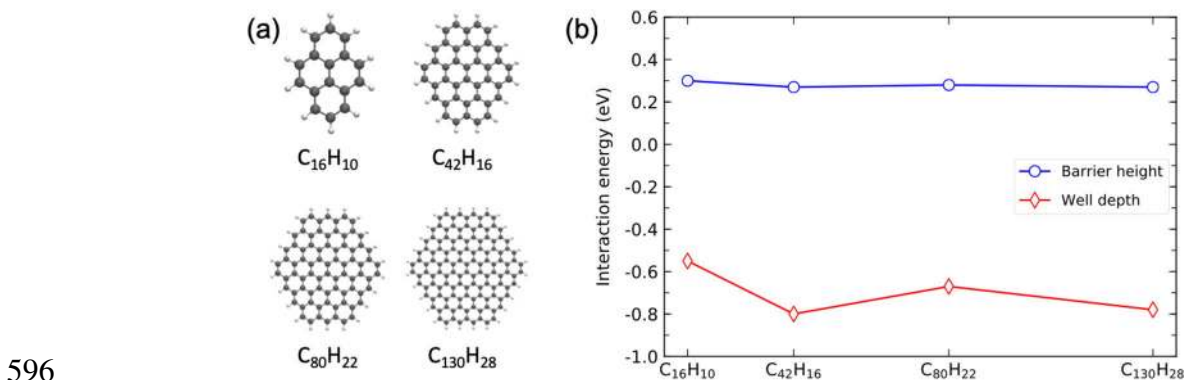


Figure S3. Graphene flake size dependence of chemisorption barrier height and well depth calculated at DFT B3LYP/cc-pVDZ level of theory. (a) graphene flakes studied in this work; (b) calculated chemisorption barrier height and well depth for different sizes of graphene flakes. All geometries are optimized at the DFT B3LYP/cc-pVDZ level of theory.

597

598

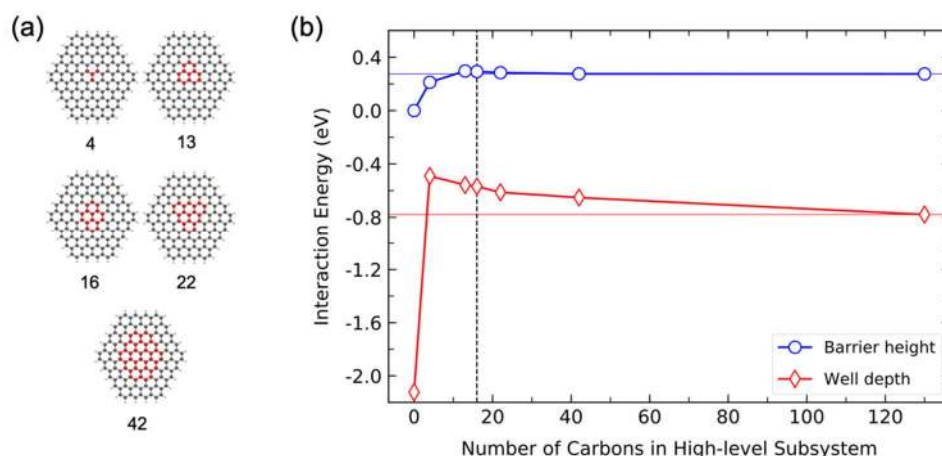


Figure S4. Accuracy of EMFT in chemisorption barrier height and well depth for the $C_{130}H_{28}$ graphene flake, relative to DFT B3LYP/cc-pVDZ level of theory. (a) Illustration of the different choices for the high-level subsystem that are considered; (b) EMFT barrier heights and well depths for different choices of the high-level subsystem. The blue horizontal line and red horizontal line correspond to DFT barrier height and well depth obtained at B3LYP/cc-pVDZ level of theory, respectively. The vertical dashed line corresponds to the high-level subsystem consisting of 16 carbon atoms. The relevant geometries are optimized at the B3LYP/cc-pVDZ level of theory.

599



Figure S5. Partitioning of the $C_{42}H_{16}$ graphene flake for EMFT calculations. The atoms in red correspond to the high-level subsystem, and the remaining atoms correspond to the low-level subsystem. The carbon atom to which the H atom binds is highlighted.

Table S2. Timing comparison on single-point energy calculations using DFT and EMFT for H on $C_{42}H_{16}$ graphene flake.^{a, b}

Method	Total time (seconds)	Relative speed-up
DFT ^c	521	1
EMFT	46	11.3

600 ^a Both calculations are performed using the same geometry optimized at the B3LYP/cc-pVDZ level of
 601 theory. For both calculations, convergence is achieved within 21 SCF iterations.

602 ^b Calculations are run on a NERSC Haswell computer with 32 cores and 128 GB DDR4 2133 MHz
 603 memory. Wall-clock times are reported.

604 ^c DFT calculation on full $C_{42}H_{16}$ flake at B3LYP/cc-pVDZ level of theory.

605 *Computational Details. 3. Fitting REBO using EMFT molecular dynamics simulations.*
606 *Ab initio* molecular dynamics (AIMD) simulations for the scattering experiment using EMFT
607 provide reference energies and forces for training of the REBO potential. The $C_{42}H_{16}$ flake is
608 used as the model system for graphene. We employ the EMFT subsystem partitioning with
609 the high-level subsystem comprised of the colliding H atom and the 16 carbon atoms (Fig.
610 S5). Initial conditions for AIMD trajectory calculations are set to mimic the experimental
611 conditions and to sample the configuration space needed for parameterization of the REBO
612 potential. These conditions include: (1) the initial coordinates and velocities of the graphene
613 atoms, which are sampled from a pre-equilibrated trajectory of the graphene at 300K using
614 Andersen thermostat; (2) the initial kinetic energy of the incident H atom is set to 1.92 eV;
615 (3) the target positions of the incident H atom are randomly distributed within the central unit
616 cell of the graphene flake; (4) the incident polar angles of the H atom range from 0° to 60°
617 with 10° spacing; (5) the incident azimuthal angles range from 0° to 180° with uniform ran-
618 dom distribution and (6) the initial H atom position is set 5 Å above the graphene surface.

619 In addition to the above trajectories, we also carry out simulations that start from the same
620 initial conditions except that the initial H atom is put 1.2 Å above the graphene surface, in
621 order to provide sufficient sampling for configurations that are near the chemisorption well
622 and barrier. A total number of ~ 400 EMFT trajectories were performed and 1600 data points
623 were used for the REBO parameterization.

624 The fit itself was performed with all three parts of the REBO PES, i.e., the C-C interaction,
625 the projectile-graphene interaction, and the interaction between the graphene flake and its
626 terminal H-atoms, being simultaneously fit. The parameters for the projectile H-atom and the
627 graphene terminal H-atoms were treated separately, to avoid having the large number of ter-
628 minal H-atoms unduly dominate the fitting; furthermore, the interaction between the graphene
629 flake and its terminal H-atoms can be disregarded when performing MD simulations with
630 periodic boundary conditions which eliminate the graphene terminal H-atoms. The fits were
631 done with the trust-region nonlinear least squares algorithm and convergence was achieved
632 typically after 12 local optimization steps. For each fit, the initial parameters were selected by
633 applying a Gaussian blur of 15% to each REBO parameter from the original publication, re-
634 sulting in an optimization in 27 dimensions.

635 The success of the re-parametrization is judged by several criteria. First, the root mean square
636 error (RMSE) must not differ much between the training and validation data; if the RMSE to
637 the training data was much lower than to the validation data, this would indicate overfitting.

638 The selected PES has an RMSE to the training data of 169 meV and the validation data can be
639 reproduced with an RMSE of 183 meV. Second, the carbon cohesive energy should not devi-
640 ate excessively from literature values; the employed PES predicts a cohesive energy of
641 12.3 eV for a carbon atom, while literature values range from 7-9 eV (58, 59). Third, cuts
642 through certain dimensions of the PES can be compared to reference calculations (see Fig.
643 S3); the re-parametrized REBO PES should be able to accurately predict energetic changes
644 during the adsorption process, i.e., barrier height, chemisorption well depth, and the correct
645 positions of both with respect to C-H distance from a top-site on the graphene surface.

646 *Computational Details 4: Ring-polymer molecular dynamics*

647 Ring-Polymer Molecular Dynamics (RPMD) is an approximate quantum dynamical method
648 that is based on Feynman's imaginary-time path integral formulation of statistical mechanics
649 (26, 60). RPMD enables quantum simulation via direct dynamics by providing a classical
650 molecular dynamics model for the real-time evolution of a quantum mechanical system. The
651 RPMD trajectories both preserve the exact quantum Boltzmann distribution and exhibit time-
652 reversal symmetry. The method has been demonstrated for the description of dynamics asso-
653 ciated with both thermal equilibrium initial conditions (26), as well as special cases of non-
654 equilibrium initial conditions (27). In the current study, we employ the “momentum impulse”
655 non-equilibrium conditions to describe graphene sheet at thermal equilibrium at 300 K but
656 with the colliding H atom initialized with a specified incident kinetic energy (27); in this pro-
657 tocol, the internal modes for the H-atom ring polymer are initially equilibrated at a tempera-
658 ture of 300 K, while the centroid mode of the H-atom ring polymer is initialized with the ve-
659 locity corresponding to the incident kinetic energy. The simulations were found to be suffi-
660 ciently converged using 12 ring-polymer beads. The thermalized initial distribution for the
661 graphene sheet was obtained using the path integral Langevin thermostat (61). In terms of the
662 position of the H atom, the RPMD scattering trajectories were initialized in the same way as
663 for the classical MD simulations, except with the position of the classical H atom replaced by
664 the centroid position of the ring polymer, and the scattering angle and final kinetic energy for
665 the RPMD trajectories were likewise determined from the centroid of the H-atom.

666 **S2. The influence of the Pt substrate on the H atom scattering**

667 Graphene primarily interacts with a Pt(111) surface through weak dispersion forces (23). The
668 EMFT-REBO approach just described was modified to include the effect of the Pt substrate
669 on the experimental observables. The substrate was modelled in the simulations using Len-
670 nard-Jones (LJ) potential interactions with each atom in the graphene layer. Specifically, car-

671 bon atoms in the graphene layer experience pair-wise interactions with a single layer of Pt
 672 atoms that simulates the surface, via a potential of the form $V(r)=4\epsilon*[(\sigma/r)^{12}-(\sigma/r)^6]$, where r is
 673 the Pt-C distance, $\epsilon = 250$ K and $\sigma = 2.95$ Å. This choice of parameters yields an interaction
 674 energy between the Pt and graphene layers of 70 meV per C atom, which is consistent with
 675 literature values (62).

676 Figure S6 shows the influence of this model of Pt-graphene interactions on the sticking prob-
 677 abilities. For both incidence energies studied in this work, the sticking probability is slightly
 678 enhanced at low E_I and slightly reduced at high E_I . For a finite surface temperature puckering
 679 is enhanced compared to free-standing graphene by the asymmetry of the LJ potential. This
 680 permits H atoms to more easily overcome the adsorption barrier. Indeed, when all degrees of
 681 freedom are allowed to relax, the minimum energy path to adsorption takes place over a barri-
 682 er that is 60 meV lower than on free-standing graphene. Meanwhile, the pre-puckering also
 683 results in a slightly smaller energy loss resulting in slightly less sticking at high E_n .

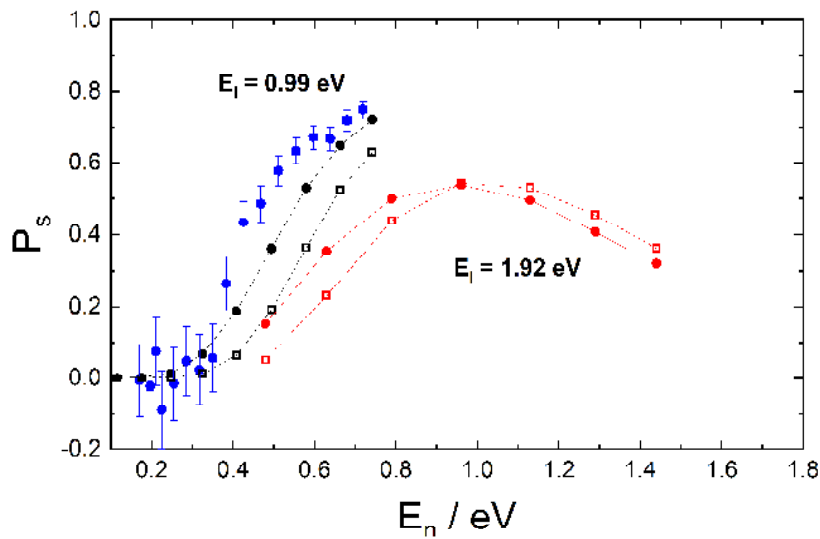
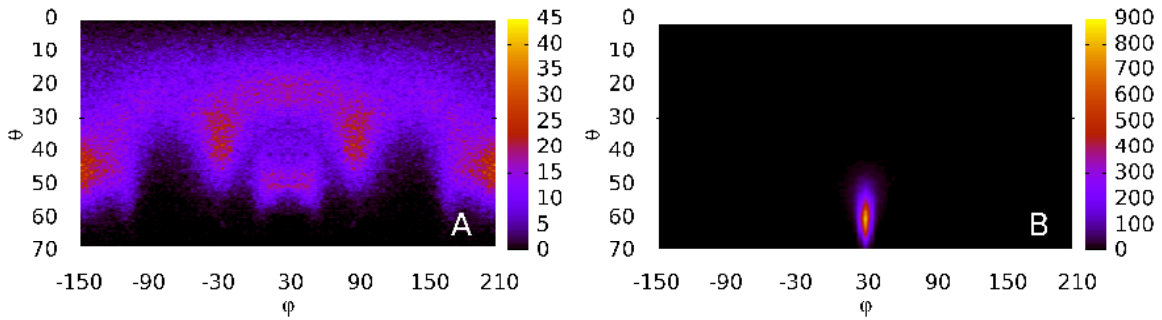


Figure S6: Influence of Pt substrate on sticking probability. Experimentally derived (blue) and theoretically predicted (black) sticking probabilities for $E_I = 0.99$ eV at various incidence angles in units of normal incidence energy (E_n). Results are for two cases: neglect of Pt (dashed lines, open symbols) versus inclusion of Pt by Lennard-Jones potential of van der Waals forces (solid lines, solid symbols). For $E_I = 1.92$ eV, the corresponding theoretical sticking probabilities are also presented (red), both neglecting (dashed lines, open symbols) and including (solid lines, solid symbols) the Pt substrate.

684 S3. Out-of-detection-plane scattering

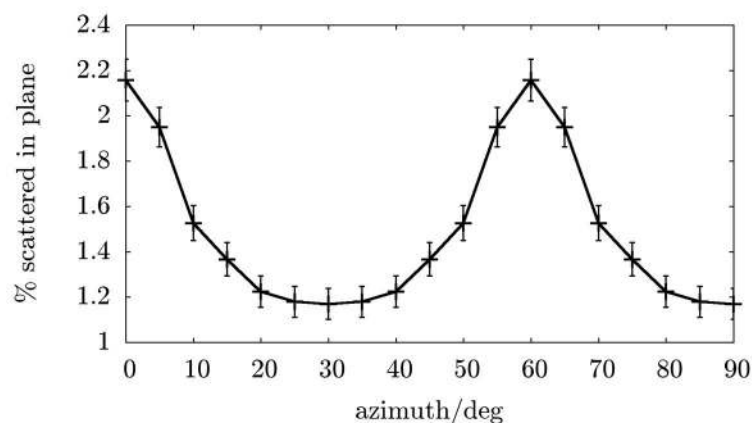
685 The experimental data is only sensitive to H atom scattering that occurs in a detection plane
 686 containing a vector along the initial H atom beam direction and a vector pointing from the H
 687 atom impact point on the graphene sample to the detector. The normal vector of this detection

688 plane is parallel to the rotation axis of the detector. Figure S7 shows representations of scat-
 689 tering simulations demonstrating the importance of scattering outside of the instrumental de-
 690 tection plane. Here, the instrument detection plane corresponds to all values of ϑ where
 691 $\varphi = 30^\circ$.



692 **Figure S7: Azimuthal scattering fluxes calculated from MD on the EMFT-REBO PES**
 693 **assuming a single rotational orientation of the graphene crystal.** Here the initial condi-
 694 tions are: $E_I = 1.92$ eV, $T_S = 300$ K. (A) **transient chemical bond formation channel** exhibit-
 695 ing scattering outside of the detection plane, $\vartheta_I = 30^\circ$, $\varphi_I = 30^\circ$, and (B) **quasi-elastic chan-**
 696 **nel** exhibiting scattering primarily within the detection plane $\vartheta_I = 60^\circ$, $\varphi_I = 30^\circ$. $\varphi_I = 0^\circ$ cor-
 698 responds to H atom trajectories whose velocity vector projection onto the graphene plane
 699 aligns with a C=C. $\varphi_I = 30^\circ$ corresponds to H atom trajectories whose velocity vector projec-
 700 tion onto the graphene plane aligns perpendicular with a C=C.
 701

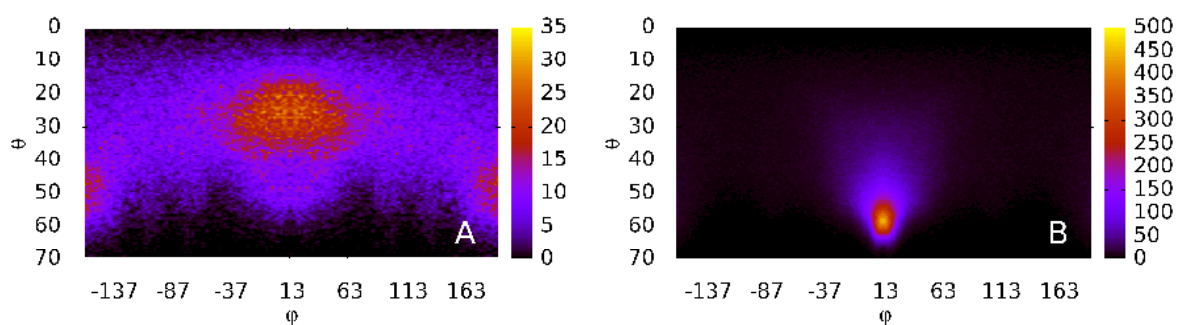
702 For the slow channel where a transient chemical bond is formed, the MD calculations on the
 703 EMFT-REBO PES show significant scattering probabilities out of the detection plane, when
 704 the incidence angle $\vartheta_I = 30^\circ$ & $\varphi_I = 30^\circ$ (see Fig. S7-A). At this value of φ_I , the projection of
 705 the H atom velocity vector onto the graphene plane is orthogonal to C=C bonds. The calcula-
 706 tions predict a large amount of H atom flux out of the detection plane by this oriented colli-
 707 sion. By contrast, the quasi-elastic channel shown in Figure S7-B, does not show this effect;
 708 here, $\vartheta_I = 60^\circ$ & $\varphi_I = 30^\circ$ mainly gives rise to scattering within the detection plane. A similar
 709 behavior can also be seen in theoretical predictions of the φ_I -dependence of the in-plane scat-
 710 tering probability, Fig. S8. In-plane scattering is largest when the projection to the incident H
 711 atom trajectory on the graphene plane aligns with a C=C and it is smallest, when the trajecto-
 712 ry is aligned orthogonal to C=C bonds.



713

714 **Figure S8: Azimuthal dependence of the in-plane signal.** Crosses are calculated values and error
 715 bars indicate the 95% confidence interval. 0° and 60° are parallel to C=C bonds, and 30° and 90° are
 716 orthogonal to them. Incidence conditions are $E_I=1.92$ eV, $\vartheta_I=45^\circ$, where changes in the in-plane signal
 717 can be attributed to out-of-plane deflection during transient bond formation.
 718

719 The graphene samples used in the experiments are not single crystals; they are composed of
 720 two equally abundant orientational domains, one rotated by 27° with respect to the other.
 721 Each domain has an orientational distribution of Gaussian with a width of $\sim 5^\circ$. The experi-
 722 mental data was acquired with $\varphi_I=13.5^\circ$, where the H atom velocity vector is oriented sym-
 723 metrically with respect to these two orientational domains. To simulate experimental results,
 724 both on sticking probabilities for $E_I=1.92$ eV presented in Fig. 3 and measured scattering
 725 fluxes shown in Fig. 2, we have carried out calculations averaging over two rotational do-
 726 mains oriented with $\varphi_I=13.5^\circ$. Figure S9 shows how the out of plane structure in the scatter-
 727 ing angular distributions is averaged out in scattering through the two domains.

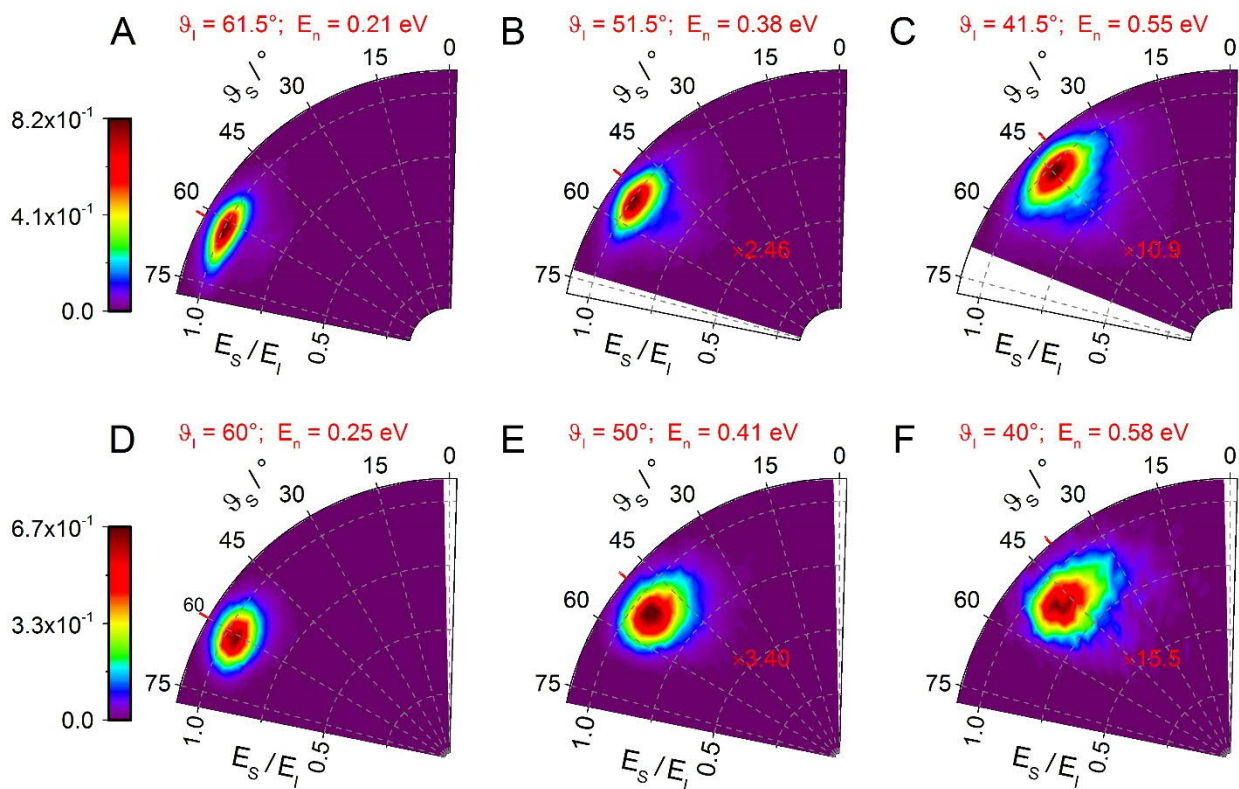


728

729 **Figure S9: Scattering fluxes calculated from MD on the EMFT-REBO PES averaging over two**
 730 **orientational domains of the graphene crystal. (A) transient chemical bond formation channel**
 731 **present at $\vartheta_I=30^\circ$ exhibiting scattering outside of the detection plane and (B) quasi-elastic channel**
 732 **seen at $\vartheta_I=50^\circ$ exhibiting scattering primarily within the detection plane. Here the initial conditions**
 733 **are: $E_I=1.92$ eV, $\varphi_I=13.5^\circ$, $T_S=300$ K. The mechanical influence of the Pt-substrate was also taken**
 734 **into account (see Sec. S2).**

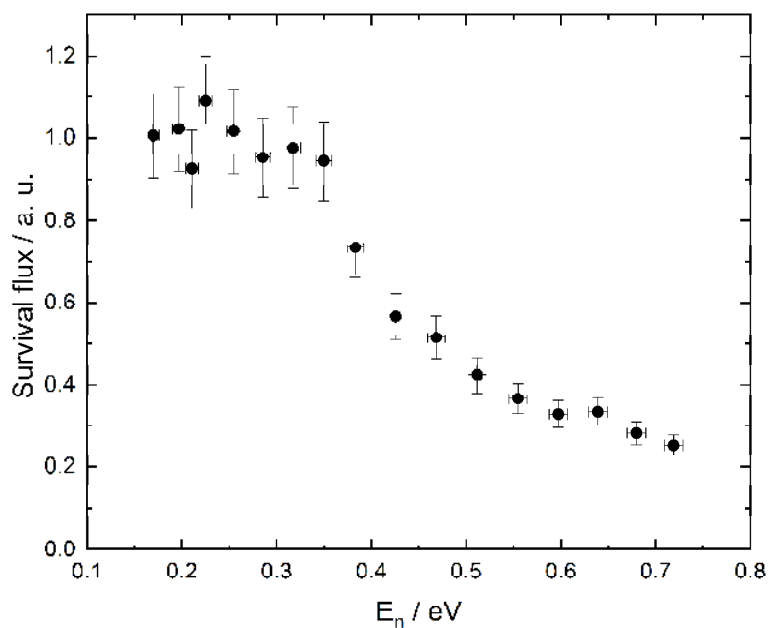
735 **S4. H atom sticking probabilities at $E_I = 0.99$ eV**

736 It is best to attempt an experimental determination of sticking probabilities where the scatter-
 737 ing in the slow channel is unimportant, otherwise a careful and accurate accounting of out of
 738 detection plane scattering must be a part of the analysis. By lowering the incidence energy to
 739 $E_i = 0.99$ eV, where no slow channel is observed, we are able to observe the survival probab-
 740 ility of the quasi-elastic channel as a function of normal incidence energy. Figure S10 shows a
 741 comparison of experiment and theory for $E_i = 0.99$ eV at three incidence angles. No slow
 742 channel is seen because the energy dissipation for low energy H atoms that cross the barrier to
 743 C-H bond formation is so efficient that re-crossing and escape back to the gas-phase does not
 744 occur. We can then use the experimental data to obtain the integrated scattered flux in the fast
 745 channel as a function of incidence angle, which is shown in Fig. S11. The survival probability
 746 increases as the normal component of incidence energy drops, reaching a plateau below $E_n =$
 747 0.35 eV. Here we set the survival probability to 1 and use this to extract the sticking probab-
 748 ility shown in Fig. 3 of the main text.



749

Figure S10: Scattering distributions of H collisions with graphene at $E_I = 0.99$ eV. A-C show measured H atom scattering energy, E_S , and angular, ϑ_S , distributions. Each distribution is multiplied by the indicated red number to use the same color bar. D-F show corresponding simulated scattering distributions. The incidence angles, ϑ_I and normal incidence energy, E_n , are also indicated $\vartheta_S = 0$ indicates the surface normal direction. Red ticks indicate the specular scattering angles. All observed scattering occurs within the plane defined by incident H atom beam and the surface normal.

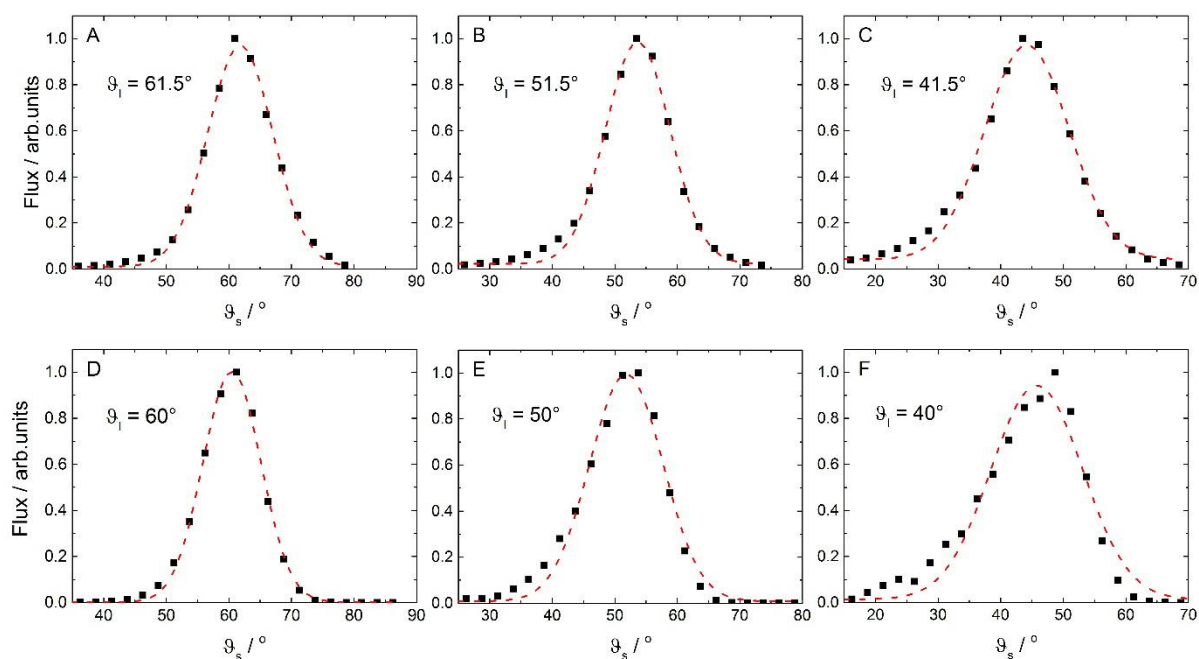


750

Figure S11: Experimentally derived survival flux using the data like that shown in Fig. S10.

751

752 This procedure requires an accounting of how the scattering angular distribution changes with
 753 incidence angle. The angular distributions in the plane of detection are shown in Fig. S12A-C
 754 (experiment) and S12D-F (theory).

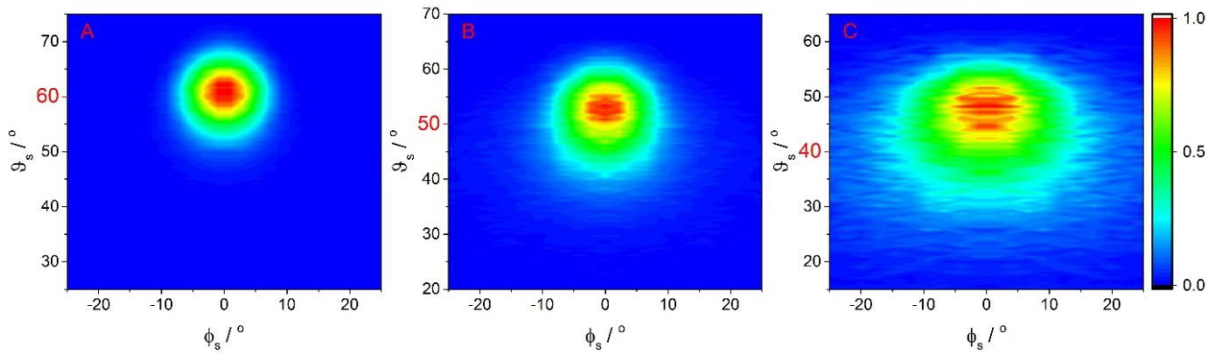


755

Figure S12: Experimental (A-C) and Theoretical (D-F) angular distribution of H atom scattering from graphene integrated over energy loss. The incidence conditions are the same with Fig. S10. Red dashed lines are Gaussian fits.

756

757 We integrate over the out-of-detection plane angles assuming cylindrical symmetry of the
758 angular distributions; Fig. S13 shows theoretical predictions that justify this assumption.

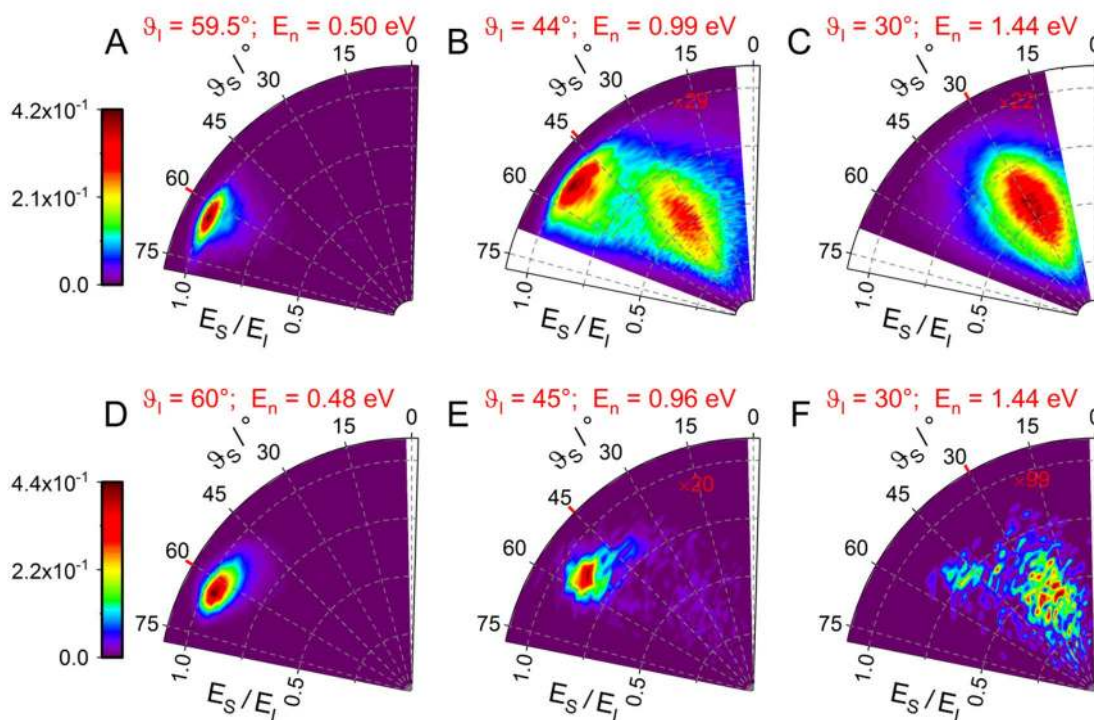


759

Figure S13: Calculated in-plane and out-of-plane angular distribution of H atom scattering from graphene integrated over energy loss. The incidence conditions are the same with Fig. S10 D-F. ϕ_s is the angle of the scattering direction relative to the plane defined by the incidence beam and surface normal. Scattering at $\phi_s = 0^\circ$ corresponds to in-plane scattering.

760 **S5. A critical comparison of experiment and theory**

761 In Figure 2 of the main text, we uniformly shifted the simulated scattering flux distributions
762 by 10° in order to emphasize the similarities between the experiment and simulations. Figure
763 S14 shows the same comparison as in Fig. 2 without the 10° shift; here, incidence angles dif-
764 fer by less than 1° . The simulation agrees well with experiment at angles where only one
765 channel is present: $\vartheta_l = 60^\circ$ shows only the fast channel and $\vartheta_l = 30^\circ$ only slow channel. For
766 the intermediate angle, both channels are present in simulations and experiment, but the simu-
767 lations overestimate the fast component's relative contribution to the scattering signal.



768

Figure S14: Scattering distributions of H collisions with graphene. A-C show measured H atom scattering energy, E_S , and angular, ϑ_S , distributions with $E_I = 1.92$ eV scattering. Each distribution is multiplied by the indicated red number to use the same color bar. D-F show corresponding simulated scattering distributions. The incidence angles ϑ_I and normal incidence energy, E_n , are indicated. $\vartheta_S = 0$ indicates the surface normal direction. Red ticks indicate the specular scattering angles. All observed scattering occurs within the plane defined by incident H atom beam and the surface normal.

769 These observations also appear in the angle-integrated energy loss distributions - Fig. S15.
 770 Again, there is excellent agreement between the simulations and experiment at $\vartheta_I = 60^\circ$ and
 771 30° , while the intermediate angle is biased towards the fast component.

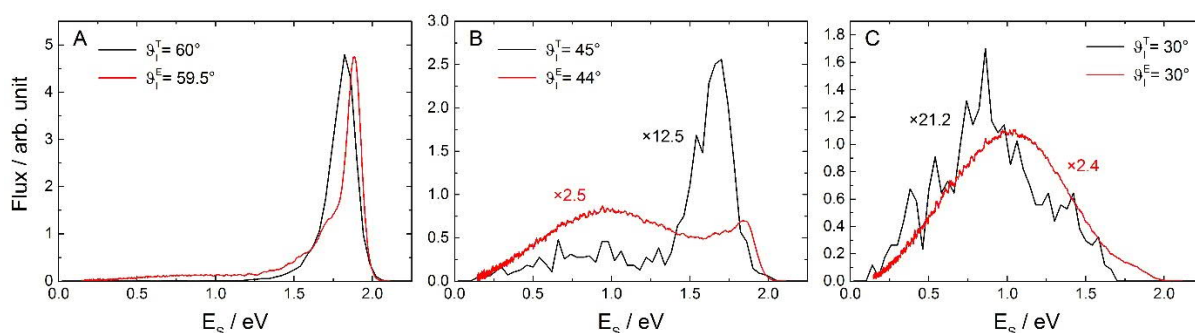


Figure S15: Energy distribution for H atom scattering within the detection plane integrated over all polar scattering angles. The incidence conditions are the same with Fig. S14. ϑ_I^T and ϑ_I^E are incidence angles for theoretical simulation and experimental measurement, respectively. The multiplying factor indicates the signal drop.

772

773 The results in both Figs. S14 and S15 suggest that, despite broad agreement between the
 774 simulations and experiment, the simulations predict a slightly higher energy threshold for C-H

775 bond formation than is seen in experiment. Evidence of this bias also appears in the predicted
776 sticking probabilities shown in Fig. 3, with the simulations requiring slightly more incidence
777 energy to overcome the barrier to C-H bond formation. These discrepancies could arise from
778 inaccuracies in the potential energy surface - possibly from the employed electronic structure
779 methods or the simplicity of the description of the Pt-graphene interactions. For example, the
780 increased degree of covalent bonding between graphene and Pt(111) that becomes possible
781 when a C-H bond is formed is not included in our treatment and will likely deepen the C-H
782 binding well and slightly lower the barrier as well.

783 Another possible source of discrepancy between experiment and simulation is the effect of
784 out-of-detection-plane scattering - see section S3. To the extent that the simulations do not
785 reproduce the scattering flux in both the fast and slow channels, the apparent branching be-
786 tween the two would differ from experiment. While the scattering effects reported here
787 emerge only from our theoretical analysis, the possible errors associated with azimuth-
788 specific scattering are likely to be small. We note that recent measurements on single crystal
789 graphene grown on Nickel show clearly that there is an influence of azimuthal incidence an-
790 gle on scattering probability (63). Moreover, the samples in the present work were polycrys-
791 talline; hence, they represent an average over two crystal orientations, an experimental condi-
792 tion that tends to wash out the influence of azimuthal specificity.

793 With these considerations in mind, we have allowed ourselves a global 10° shift in the polar
794 angle of Fig 2 to emphasize the broad similarities between the simulated and experimental
795 results. More important than the above described discrepancies, in our view, is that the ener-
796 gy loss predicted by the theory is nearly identical to that of experiment, as is clear from Figs.
797 S15 A&C. It is for this reason that excellent agreement between simulation and experiment is
798 obtained for the sticking probabilities in Fig. 3, where we duly note that no global polar angle
799 shift has been introduced.

800 **S6. Sonic wave energy transport**

801 Fig. S16 shows the time dependent displacement of carbon atoms involved most directly with
802 the H atom during the collision. As in Fig. 4, carbon atom shells are used to group neighbor-
803 ing atoms. When the H atom induced sp^2 - sp^3 re-hybridization of the 0^{th} shell C-atom occurs,
804 the length of its bonds to neighboring C atoms changes. As a consequence, the carbon atoms
805 in the 1^{st} shell are initially pushed away from the center of impact. In turn, the second shell
806 carbon atoms are also deflected. This process continues and a wave propagates through the
807 graphene sheet. By monitoring the C-atom's displacements during simulation, we calculate

808 the speed of this wave to be ~ 18.6 km/s. This is similar to graphene's in-plane speed of sound
 809 (22 km/s) determined by analysis of the LA phonon branch (29). This agreement with our
 810 simulations also argues for the overall accuracy of our EMFT-REBO PES.

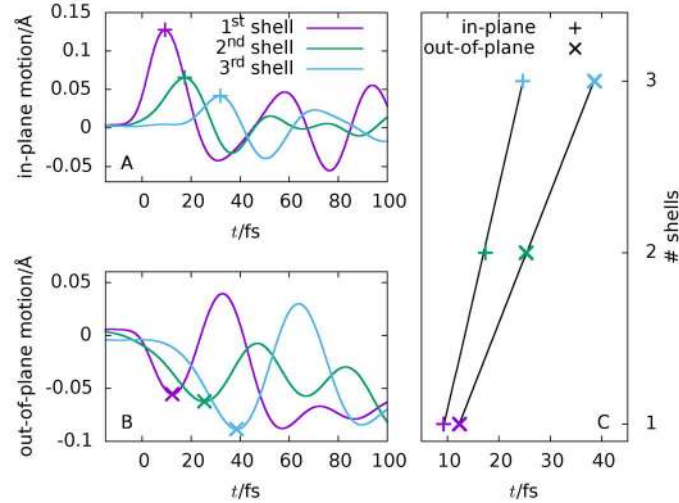


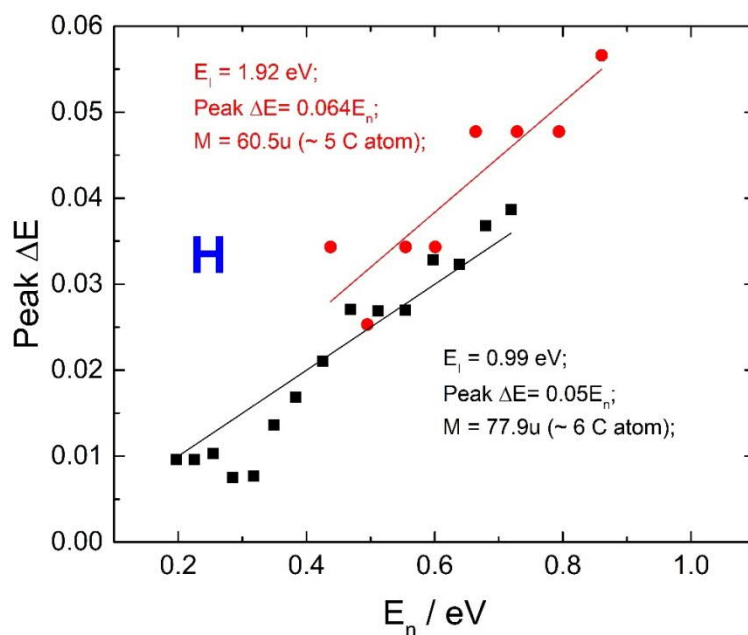
Figure S16: Sonic wave energy dissipation. **A)** In-plane deflection of C-atoms in different shells from their respective equilibrium distance to the C-atom struck by the projectile. The maximum amplitudes are marked by pluses. Time zero is defined as the time of H atom closest approach. These results are the average of the 60 selected trajectories shown in Fig. 4B. **B)** Out-of-plane deflection of the carbon atoms in the same shells as in panel A. **C)** Points in time when the marked extrema in panel A and B are observed. From a least squares fit the speed of the outgoing waves is calculated to be 18.6 km/s in-plane and 10.9 km/s out-of-plane.

811 **S7. The hard cube model, the quasi-elastic channel and the site specificity of sticking**

812 Figure S17 shows a dynamical feature of the fast channel observed in this study that is mark-
 813 edly different from the dynamics of the slow channel. Here, we compare predictions of the
 814 hard cube model to experimental data for the fast channel. The hard cube model envisions the
 815 H atom of mass m colliding with a flat surface of mass M at an incidence angle ϑ_I . The model
 816 conserves momentum parallel to the surface allowing one to show that the energy loss ΔE , is
 817 given by the following formula.

$$\Delta E = E_I - E_S = \left[\frac{4Mm}{(M+m)^2} \right] E_I \cos^2 \vartheta_I = \left[\frac{4Mm}{(M+m)^2} \right] E_n$$

818 Here M is the only adjustable parameter to fit the data (the red and black solid lines in Fig.
 819 S17).



820

Figure S17: Most probable energy loss for the fast channel at various incidence angles in units of normal incidence energy E_n . Solid lines are fittings according to a hard cube model. Symbols are derived from experiment.

821

822 The effective mass of the hard cube, M , is close to the mass of 5-6 Carbon atoms. This sug-
 823 gests that for the quasi-elastic channel, the H atom interacts with a six membered ring of C-
 824 atoms.

825 The site-specific sticking probabilities, shown in Figure S18 for several incidence energies
 826 help to explain this. At $E_n = 0.5$ eV, sticking is more likely for collisions directly over C-
 827 atoms, where the barrier is lowest. Conversely, quasi-elastic scattering occurs when H atoms
 828 collide away from C-atoms, that is, for collisions over the center of the six membered rings.
 829 As the incidence energy increases to $E_n = 1$ eV, the sit-specific restrictions for sticking relax.
 830 Conversely, the site specificity of the quasi-elastic channel increases. Here, the quasi-elastic
 831 channel results from an impact precisely at the center of a six membered C-ring, where the H
 832 atom is simply too far from any C atom to interact specifically with a single atom. Instead, the
 833 picture emerges that the quasi-elastic channel resembles a collision with a rigid six membered
 834 C atom ring.

835

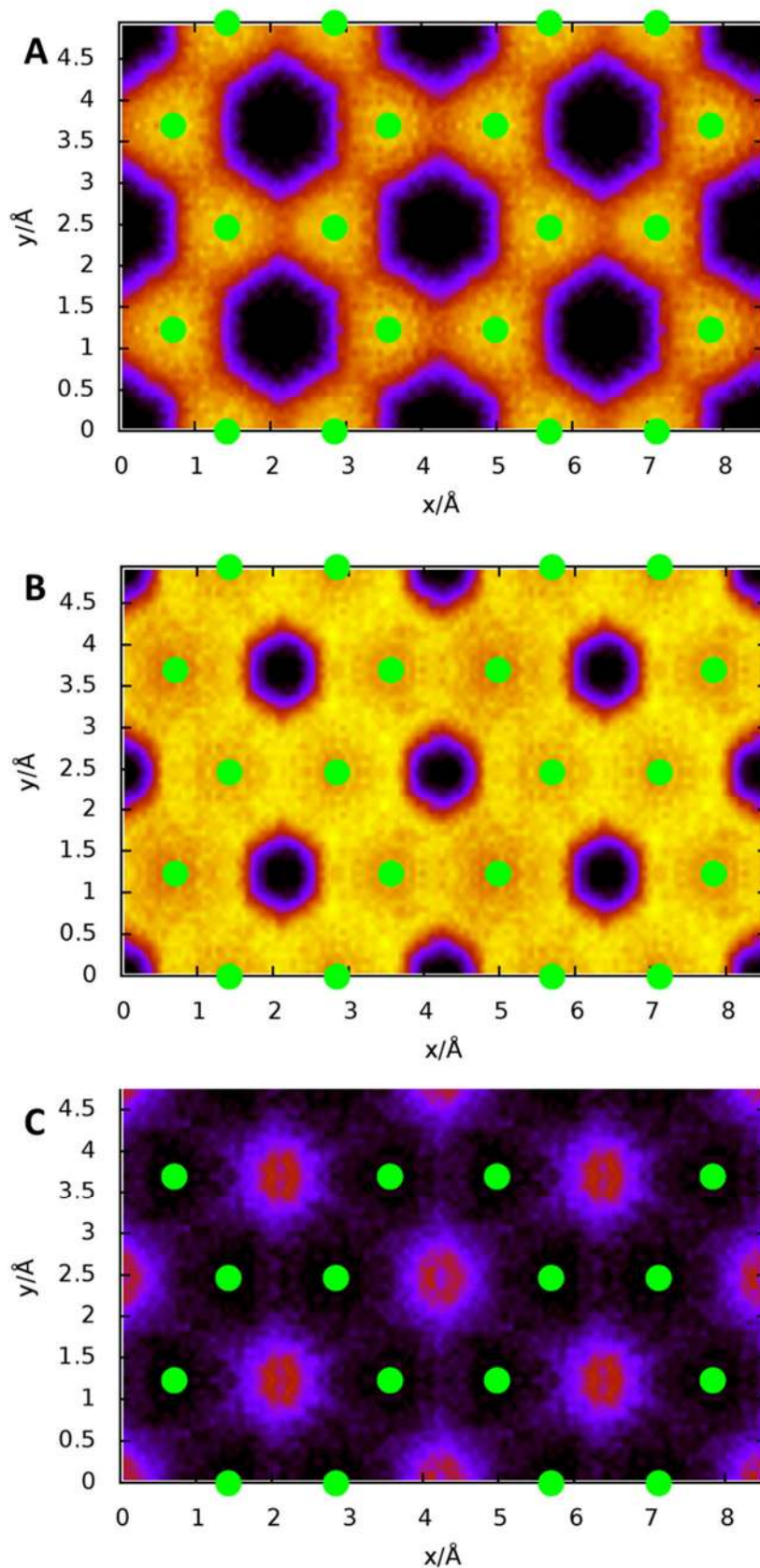


Figure S18: Heat Map representation of the site specific sticking of H atoms at graphene versus H atom incidence energy. A) $E_I = 0.5$ eV (near threshold). B) $E_I = 1.0$ eV (sticking probability maximum). C) $E_I = 2.0$ eV (incidence energy too high for efficient sticking). Incidence direction is along the surface normal. Green filled circles indicate position of C atoms. Increasing brightness of the color denotes increasing sticking probability.

836 At high incidence energies sticking and slow channel scattering dominate and compete with
 837 one another. It is easy to understand that at $E_I = 0.5$ eV, only H-atoms that directly collide on
 838 top of C atoms can stick. Top sites have the smallest adsorption barrier height and H atoms
 839 that collide on other sites do not have enough energy to overcome the barrier. Furthermore,
 840 the H atoms that pass over the barrier have low energies that dissipate rapidly into the gra-
 841 phene. At high incidence energies, crossing the barrier is necessary but not sufficient for
 842 sticking; dissipating the excess energy is also necessary. As can be seen in Fig. S18, directly
 843 hitting the C atom no longer leads to the maximum probability for H atom sticking. In fact, at
 844 $E_I = 2.0$ eV, sticking is only possible when the H atom avoids the top site. This allows some
 845 of the normal incidence energy to be channeled into kinetic energy parallel to the surface, an
 846 effect that suppresses re-crossing of the barrier.

847 S8. Comparison to previous sticking probability work

848 Figure S19 compares the sticking probabilities emerging from our experimentally validated
 849 first principles calculations to those previously reported. The four previous reports all show
 850 lower sticking probability than is found in this work. This deviation is larger at higher inci-
 851 dence energies.

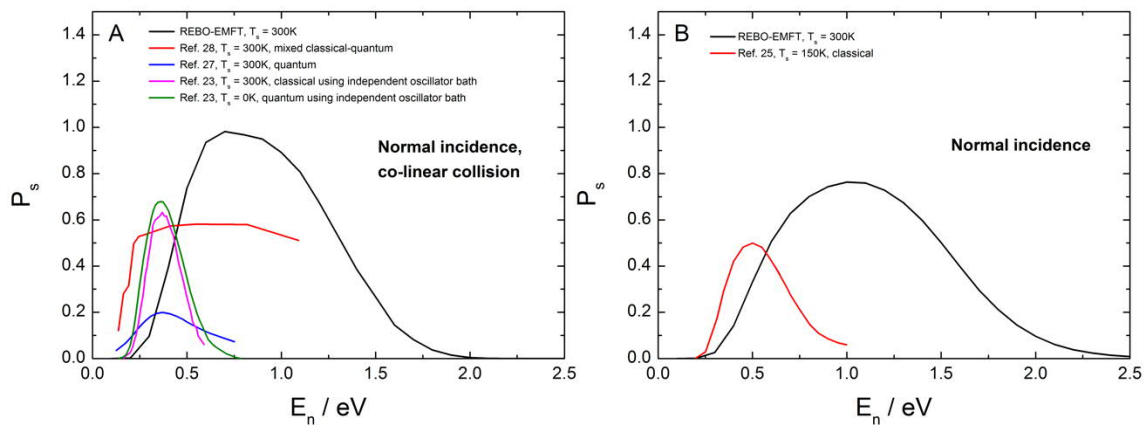


Figure S19: Comparison of theoretically predicted H sticking probabilities on graphene. **A** shows the H atom sticking probability for normal incidence and co-linear collision. T_s indicates the surface temperature in the simulation. E_n indicates the normal incidence energy (also the incidence energy). **B** shows the H atom sticking probability for normal incidence, and averaged over all impact parameters.

852 All of the methods (except that of Lemoine) appear to overestimate the sticking probability at
 853 low energy and all methods underestimate the sticking probability at high energy. While the
 854 previous studies all used different approaches, in light of the present work they all suffer from
 855 a common flaw: they only consider the Z direction movement of the C atoms. Some also only
 856 consider the Z motion of the H atom as well. In short, all of these approaches used reduced

857 dimensionality approximations that explicitly ignore concerted in-plane C-atom motion that
858 leads to the high H atom translational inelasticity seen in this work. In fact, even the most
859 recent reduced dimensionality theory agrees well with an impulsive collision model (28). This
860 differs starkly from the dynamics seen in our work. Furthermore, the use of DFT at the GGA
861 level to obtain input about the potential energy surface clearly results in a barrier to C-H bond
862 formation that is too low - this is likely the explanation for the overestimated sticking proba-
863 bility at low energy seen in several of the studies.

864 **S9. Classical simulations of IVR lifetimes**

865 Conventional IVR experiments utilize optical excitation of a molecule initially at its equilibri-
866 um configuration. For the H graphene system, we seek to simulate such an experiment by
867 initiating classical trajectories from an initial geometry that differs from the minimum energy
868 structure only by the displacement of the H atom. This initial state resembles one produced by
869 pumping a high overtone of the C-H stretch. To describe this, we set up the following simula-
870 tion.

871 H adsorbed on a graphene surface is equilibrated in phase space to 300 K using the Andersen
872 thermostat (64) in an NVT ensemble. Next, an NVE ensemble is simulated for 100 ps from
873 which a snapshot is taken every 100 fs. Then, in each of the 1000 snapshots, the H atom is
874 relaxed to the chemisorption well via the FIRE algorithm (65) while keeping all other degrees
875 of freedom fixed. This completes the stage of preparation of an ensemble of initial conditions
876 for the C atoms. Then for each initial total energy, we run 4500 NVE trajectories for 10 ps. A
877 trajectory is initialized by first selecting one of the geometry-optimized snapshots and displac-
878 ing the H-atom a certain distance either towards or away from the closest C-atom. This dis-
879 tance is randomly drawn from a uniform distribution ranging from -0.2 to 0.2 Å. Next, the
880 change in potential energy is calculated and if it is lower than the total energy of the simula-
881 tion, the geometry is accepted and the remaining energy is provided as kinetic energy to the
882 H-atom, letting its initial velocity vector randomly either point towards the graphene sheet or
883 away from it. Finally, the trajectory is started in the NVE ensemble and the kinetic energy of
884 the H-atom is saved every 0.1 fs. To obtain the time-scales of IVR for the set of initial kinetic
885 energies, we average the kinetic energy of the H-atom in each time step over all trajectories in
886 which it remained attached to graphene. Dissociation was observed in less than 150 trajecto-
887 ries at any initial energy and the results are shown in Fig. S20A.

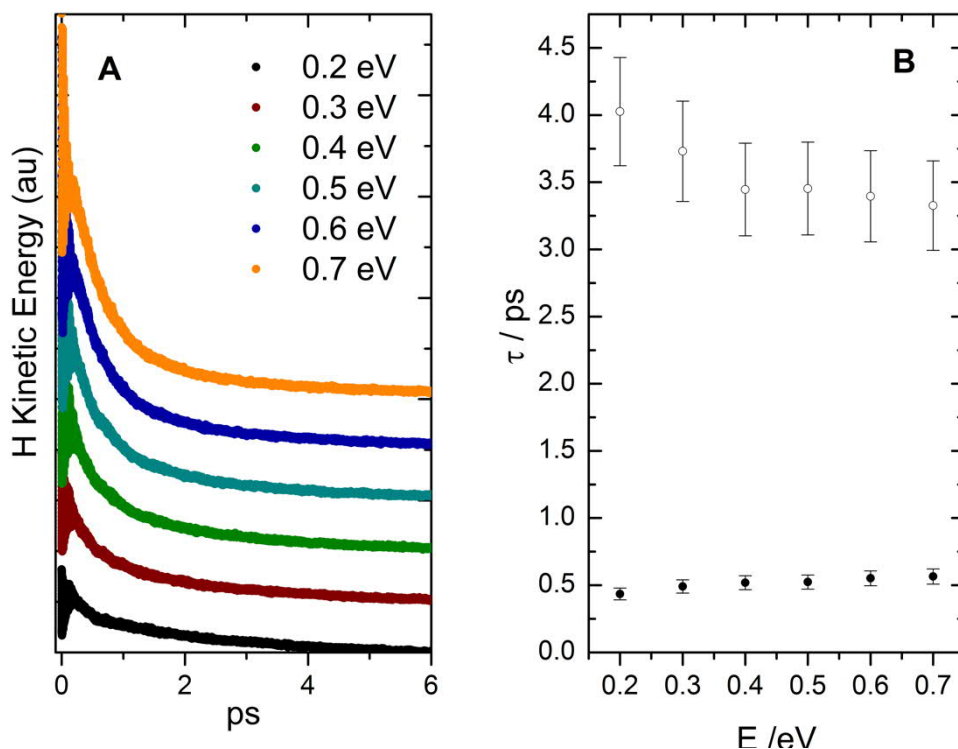


Figure S20: Classical Simulations of Intramolecular Vibrational Relaxation. **A** shows the H atom kinetic energy versus time at various initial energies. The plots are offset vertically from one another for clarity. Initially all energy is in either potential or kinetic energy of the H atom. The flow of H atom energy to the graphene slab takes place on the ps time-scale. The time dependence is best fit by a bi-exponential decay; the exponential lifetimes of the two process are shown in **B**. The error bars are estimated to be 10% of the lifetimes' values and they are mainly due to oscillations in the averaged data at early times.

888

889 The IVR follows a bi-exponential decay. It is comprised of a fast process that takes place in
 890 approximately 0.5 ps and seems to decelerate toward higher energies and slow process taking
 891 place on the order of several picoseconds- see Fig. S20B.

892